9-26-2018

The three-stage petrochemical evolution of the Steens Basalt [southeast Oregon, USA] compared to large igneous provinces and layered mafic intrusions

N. E. Moore
Oregon State University

A. L. Grunder
Oregon State University

Wendy A. Bohrson
Central Washington University

Recommended Citation

Moore, N.E., Grunder, A.L., and Bohrson, W.A., 2018, The three-stage petrochemical evolution of the Steens Basalt (southeast Oregon, USA) compared to large igneous provinces and layered mafic intrusions: Geosphere, v. 14, no. 6, p. 2505–2532, https://doi.org/10.1130/GES01665.1.

Research Paper

GEOSPHERE

GEOSPHERE; v. 14, no. 6

https://doi.org/10.1130/GES01665.1

16 figures; 2 tables; 1 set of supplemental files

CORRESPONDENCE:
mooreni@geo.oregonstate.edu

CITATION: Moore, N.E., Grunder, A.L., and Bohrson, W.A., 2018, The three-stage petrochemical evolution of the Steens Basalt (southeast Oregon, USA) compared to large igneous provinces and layered mafic intrusions: Geosphere, v. 14, no. 6, p. 2505–2532, https://doi.org/10.1130/GES01665.1.

Science Editor: Shanaka de Silva
Associate Editor: Julie Roberge

Received 8 January 2018
Revision received 23 April 2018
Accepted 7 August 2018
Published online 26 September 2018

The three-stage petrochemical evolution of the Steens Basalt (southeast Oregon, USA) compared to large igneous provinces and layered mafic intrusions

N.E. Moore[1], A.L. Grunder[1], and W.A. Bohrson[2]

[1]College of Earth, Ocean and Atmospheric Sciences, Oregon State University, 104 CEOAS Administration Building, Corvallis, Oregon 97331, USA
[2]Department of Geological Sciences, Central Washington University, 400 E. University Way, Ellensburg, Washington 98926, USA

ABSTRACT

The Steens Basalt, southeast Oregon, USA, initiated at 17 Ma as the earliest pulse of the Columbia River Flood Basalt of the northwestern USA. New and existing stratigraphically controlled data reveal temporal changes in lava flow character, and whole-rock and mineral compositions, which we use to evaluate how the balance of magma differentiation processes change in time. Temporal petrochemical variations in the Steens Basalt are analogous to the transition from Imnaha Basalt to Grande Ronde Basalt units of the Columbia River Flood Basalt and have parallels to the temporal evolution of the Deccan and Siberian traps, in India and Russia, respectively, as well as to the stratigraphic sequences of the Bushveld, of South Africa, and Stillwater, in southern Montana, USA, layered mafic intrusions. The excellent stratigraphic control from the Steens Basalt provides a detailed record for comparison across this variety of large mafic systems, providing ability to focus on commonalities among differentiation processes in time.

Chemostratigraphic excursions and volcanological characteristics in the Steens Basalt record a three-stage history. A minimally exposed early stage preserved in the lower A Steens Basalt section is characterized by heterogeneity (3–8 wt% MgO) collapsing to homogeneity (~5 wt% MgO), suggesting crystal fractionation outpaces recharge. Sparse weathering horizons indicate some time elapses between eruptions. The second stage, lower B Steens Basalt, is volumetrically dominant and represents waxing of the basaltic pulse. Flows are stacked immediately upon one another without evidence of weathering or intervening sedimentary horizons, indicating high-eruptive frequency. Compositions oscillate over a ΔMgO of ~4–5 wt% between low- and high-MgO basalt, both of which become more magnesian up section, signaling a period dominated by recharge. This stage closes with declining oscillations to produce homogeneous compositions (6–8 wt% MgO). The waning stage of eruption is represented by the upper Steens Basalt section, where thin intercalated weathering horizons occur especially high in the section. The upper Steens Basalt is characterized by overall declining MgO and increasing incompatible element concentrations confirming the dominance of crystal fractionation accompanied by crustal assimilation. In detail, the upper Steens Basalt initiates with a small stack of heterogeneous flows (5–8 wt% MgO), followed by a period of relatively homogeneous flows (~6 wt% MgO) and closes with highly variable basalts to trachybasaltic andesites. These compositional characteristics coupled with a change in average flow thickness from lower to upper Steens Basalt of <5 m to 5–10 m illustrate a shift to more silicic compositions and higher viscosity up section.

The chemical changes up section in other large igneous provinces record similar variations in differentiation processes through time, suggesting that these large volume systems share similar evolutionary histories: the earliest records suggest the magmatic systems are initially more ephemeral and compositionally variable as magma traverses relatively cool crust. With waxing, a transition to regimes of high thermal and mass input results in a stage where recharge outpaces crystal fractionation. Thermal priming of the crust during these events coupled with waning input yields magmas in which fractionation plus crustal assimilation dominates over recharge late in the system; pulses of later stage felsic magmatism in many large mafic provinces are consistent with this evolution. Using layered mafic intrusions as an analog for intrusive, cumulus-dominated residua of voluminous fractionation, as well as oceanic large igneous provinces as an analog for total magma volumes in continental flood basalt regimes, leads to the suggestion that 50%–85% of the total magma volume in a flood basalt remains in the crust, effectively remaking the crust in these regions.

INTRODUCTION

The large igneous provinces (LIP) expressed as continental flood basalts (CFB) signal geologically short-lived, catastrophic events with far-reaching consequences, from lava inundation of fossil landscapes to potential climatic effects and mass extinctions (e.g., Hofmann, 1997; Self et al., 2006; Whiteside et al., 2010). CFB are generally less voluminous and cover smaller areas than oceanic LIP (Fig. 1; Coffin and Eldholm, 1994; Coffin et al., 2006). Unlike their oceanic counterparts, CFB are filtered through several tens of kilometers of continental crust prior to eruption. If the melting anomalies that drive both con-

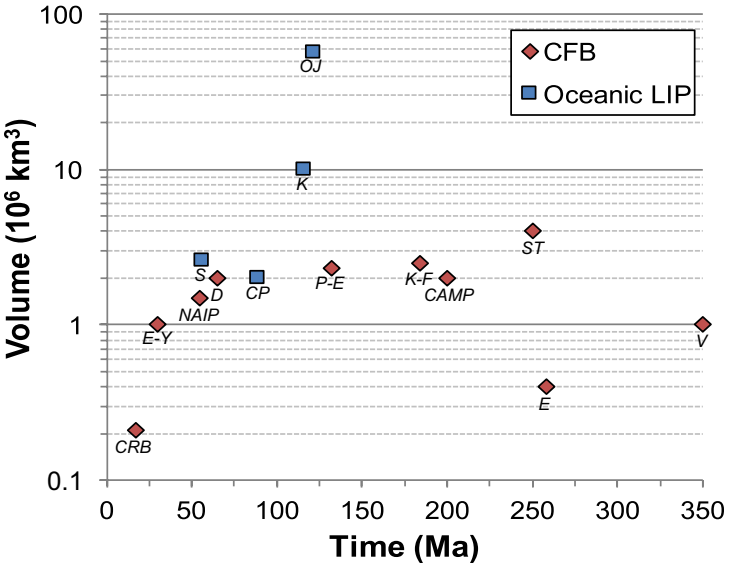

Figure 1. Volume versus age record of Phanerozoic continental flood basalt (CFB) and oceanic large igneous provinces (LIP) for select major provinces. Volume and age estimates from Courtillot and Renne (2003), Rampino and Self, 2015, and Wells et al. (2014). The Precambrian Keweenawan Province (1100 Ma), though well outside of this timespan, plots near the volumetric average of Phanerozoic LIP (~2 × 10⁶ km³). CAMP—Central Atlantic Magmatic Province; CP—Caribbean Plateau; CRB—Columbia River Basalt (including the Steens Basalt); D—Deccan Traps; E—Emeishan Traps; E/Y—Ethiopia/Yemen CFB; K—Kerguelen Plateau; K/F—Karoo/Ferrar Provinces; NAIP—North Atlantic Igneous Province; OJ—greater Ontong Java (Ontong Java, Manihiki, and Hikurangi plateaus, South Pacific Ocean); P/E—Paraná/Etendeka Traps; S—Siletzia-Crescent Terrane; ST—Siberian Traps; V—Viluy Traps (Russia).

tinental and oceanic LIP are comparable, then a substantial amount of magma is sequestered as intrusions during CFB magmatism. CFB volumes appear to have been generally consistent in time over the past 350 Ma, with most on the order of 1–3 × 10^6 km^3 (Fig. 1; Courtillot and Renne, 2003). The maximum volume, >3 million km^3, is found in the Triassic Siberian Traps, Russia (250 Ma), coinciding with initiation of the breakup of Pangaea. The smallest, with an estimated volume of 210,000 km^3, is the Neogene Columbia River Basalt Group (CRBG; ca. 16.8–6 Ma) that lies across parts of the northwestern USA. On the other hand, it has been proposed that the Siletzia-Crescent Terrane (Fig. 1), in western Washington and Oregon, USA and British Columbia, Canada, is the oceanic LIP that represents the initiation of the Yellowstone hotspot and that the CRBG is the resurgence of that plume after the interference by the subducting slab overriding the plume (Coble and Mahood, 2012; Wells et al., 2014). The volume of the unsubducted portion of the Siletzia-Crescent Terrane is ~2.6 × 10^6 km^3, on par with most Phanerozoic CFB but far smaller than the great oceanic LIPs of Kerguelen or Ontong Java, southern Indian Ocean and South Pacific Ocean, respectively.

Many decades of work on CFB have set the stage for wrestling with the questions of how mantle-derived floods of basalt impact the crust through which they pass and how melts in equilibrium with the mantle evolve to compositions typical of CFB. Most CFB provinces include high-Mg primitive lavas, but on the whole, the bulk of CFB have compositions consistent with crustal differentiation from high-Mg melts as indicated by MgO typically less than 8 wt% and Ni generally less than 200 ppm (e.g., Cox 1980; Thompson et al., 1983; Garfunkel 2008). As a counterpoint, some workers propose that melt from substantially metasomatized mantle sources (e.g., Turner et al., 1996; Hawkesworth et al., 1999) or of eclogite account for dominant CFB compositions (e.g., Takahahshi et al., 1998; Camp and Hanan 2008; Luttinen et al., 2010).

The Columbia River Basalt Group, the youngest and smallest CFB worldwide, covers 210,000 km^2 of the Pacific Northwest (Reidel et al., 2013; Figs. 1 and 2A). The main eruptive stage spanned from ca. 17 to 15.6 Ma, but the waning stage persisted until ca. 6 Ma (Reidel et al., 1989a; Baksi, 2013; Barry et al., 2013). The CRBG lavas are dominantly basaltic andesite; the most voluminous formation, the Grande Ronde Basalt, has an average silica content of 54.3 wt% SiO_2 (n = 230; Hooper, 2000), reflective of differentiation processes that affected the basalts as they passed through the crustal filter. This is in contrast to most CFB, which are largely basaltic in composition (Fig. 3). The Steens Basalt is not only the oldest member of the CRBG but is also largely basalt (48.5–52 wt% SiO_2, Fig. 3), and thus links global CFB provinces and the differentiated bulk composition of the CRBG.

Thick sections of broadly conformable lavas of Steens Basalt record a temporal change from basaltic to basaltic andesite composition. The Steens Basalt is informally divided into a lower, more mafic and tholeiitic section that includes the most primitive basalts of the CRBG, and an upper less magnesian, mildly alkalic section more enriched in select incompatible trace elements and more crustal isotopic character (Camp et al., 2013). We explore how the temporal changes in composition reflect variation in dominant magma differentiation processes within the crust (i.e., recharge, fractional crystallization, assimilation). Our focus is how a large basaltic pulse is affected by crustal staging.

Geochemical changes in time are evident in other CFB (cf. Deccan Traps; Beane et al., 1986) as well as other voluminous mafic magmatic systems such as layered mafic intrusions (LMI) (Raedeke and McCallum, 1984; Yudovskaya et al., 2013). In this paper, we describe the textural and geochemical changes in time during the Steens Basalt eruptive event with emphasis on the lower and most mafic Steens Basalt and compare these changes to those found in the Imnaha and Grande Ronde Basalt formations of the CRBG. We explore the temporal changes in other voluminous mafic provinces with stratigraphically controlled data, including the Deccan and Siberian Traps (CFB) and LMI, comparing them with the Steens Basalt history to show relationships among the nature and evolution of magmatic processes across these various LIP settings. The detailed stratigraphic data available for the Steens Basalt sequence and interpretation of the distinct phases within serves as a baseline for comparative study to these other large mafic systems.

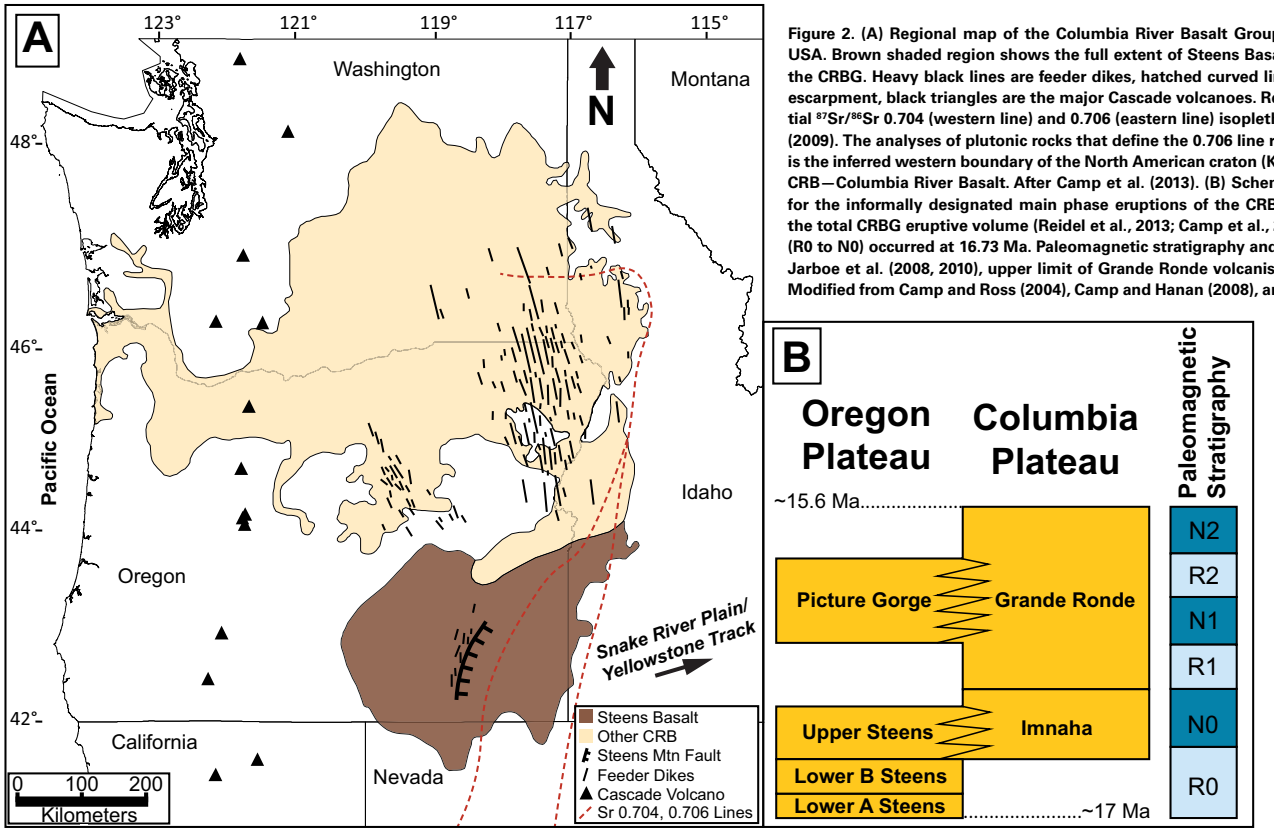

Figure 2. (A) Regional map of the Columbia River Basalt Group (CRBG) in Northwestern USA. Brown shaded region shows the full extent of Steens Basalt; tan is the remainder of the CRBG. Heavy black lines are feeder dikes, hatched curved line is the Steens Mountain escarpment, black triangles are the major Cascade volcanoes. Red dashed lines are the initial $^{87}Sr/^{86}Sr$ 0.704 (western line) and 0.706 (eastern line) isopleths from Pierce and Morgan (2009). The analyses of plutonic rocks that define the 0.706 line reflect crustal sources, so it is the inferred western boundary of the North American craton (Kistler and Peterman, 1973). CRB—Columbia River Basalt. After Camp et al. (2013). (B) Schematic regional stratigraphy for the informally designated main phase eruptions of the CRBG, that compose ~93% of the total CRBG eruptive volume (Reidel et al., 2013; Camp et al., 2013). The Steens Reversal (R0 to N0) occurred at 16.73 Ma. Paleomagnetic stratigraphy and Steens Reversal age from Jarboe et al. (2008, 2010), upper limit of Grande Ronde volcanism from Barry et al. (2013). Modified from Camp and Ross (2004), Camp and Hanan (2008), and Wolff and Ramos (2013).

GEOLOGIC SETTING

The Steens Basalt covers ~53,000 km^2 of southeast Oregon, USA, with an average thickness of 600 m (Camp et al., 2013) and has reported ages ranging from 16.8 to 16.1 Ma (Camp et al., 2013 and references therein; Mahood and Benson, 2017; all ages from these references are calibrated to Fish Canyon Tuff sanidine, in southwest Colorado, USA, standard age of 28.201 ± 0.023 Ma of Kuiper et al., 2008), making them broadly coeval with the Imnaha Basalt flows of the CRBG (Hooper et al., 2002; Fig. 2B). Steens Basalt lavas erupted within no more than 300,000 years of the Steens Mountain magnetic reversal, estimated at 16.7 Ma (Jarboe et al., 2010) and revised to 16.5 Ma (Mahood and Benson, 2017). To the south and east, "Steens-like" (basaltic andesite to andesite) lavas are as young as 15.1 Ma (Brueseke et al., 2007). The Steens Basalt crops out in a spectacular, 1-km-thick sequence of as many as 200 lava flows at Steens Mountain, most of which are relatively thin lobes (<5 m) within compound pahoehoe flows (after Walker, 1971) with lesser and thicker (5–10 m) a'a and pahoehoe single flows particularly high in the section (Bondre and Hart, 2008; Camp et al., 2013). The section is cut by NNE-striking Steens Basalt dikes exposed along the Steens Mountain escarpment (Minor et al., 1987a, 1987b; Jarboe et al., 2010; Camp et al., 2013). The Steens Basalt covers an area comparable to the combined subaerial footprint of Mauna Loa and Kilauea volcanoes, in Hawaii, USA, but at 31,800 km^3, it is only 15% of the 210,000 km^3 estimated total volume of the CRBG (Hooper et al., 2007; Camp et al., 2013). A prevalent interpretation is that the Steens Basalt is the remnant of a shield volcano (Mankinen et al., 1987; Rytuba 1988), but Bondre and Hart (2008) attribute the shield-like morphology to Basin and Range block uplift, modest tilting, and erosion. Regardless, Steens Mountain is an important volcanic locus because the basalt section there is thickest, the age record is longest, the compositional range is widest, and dikes are common. The lower Steens Basalt covers the full areal extent of Steens Basalt lavas, whereas

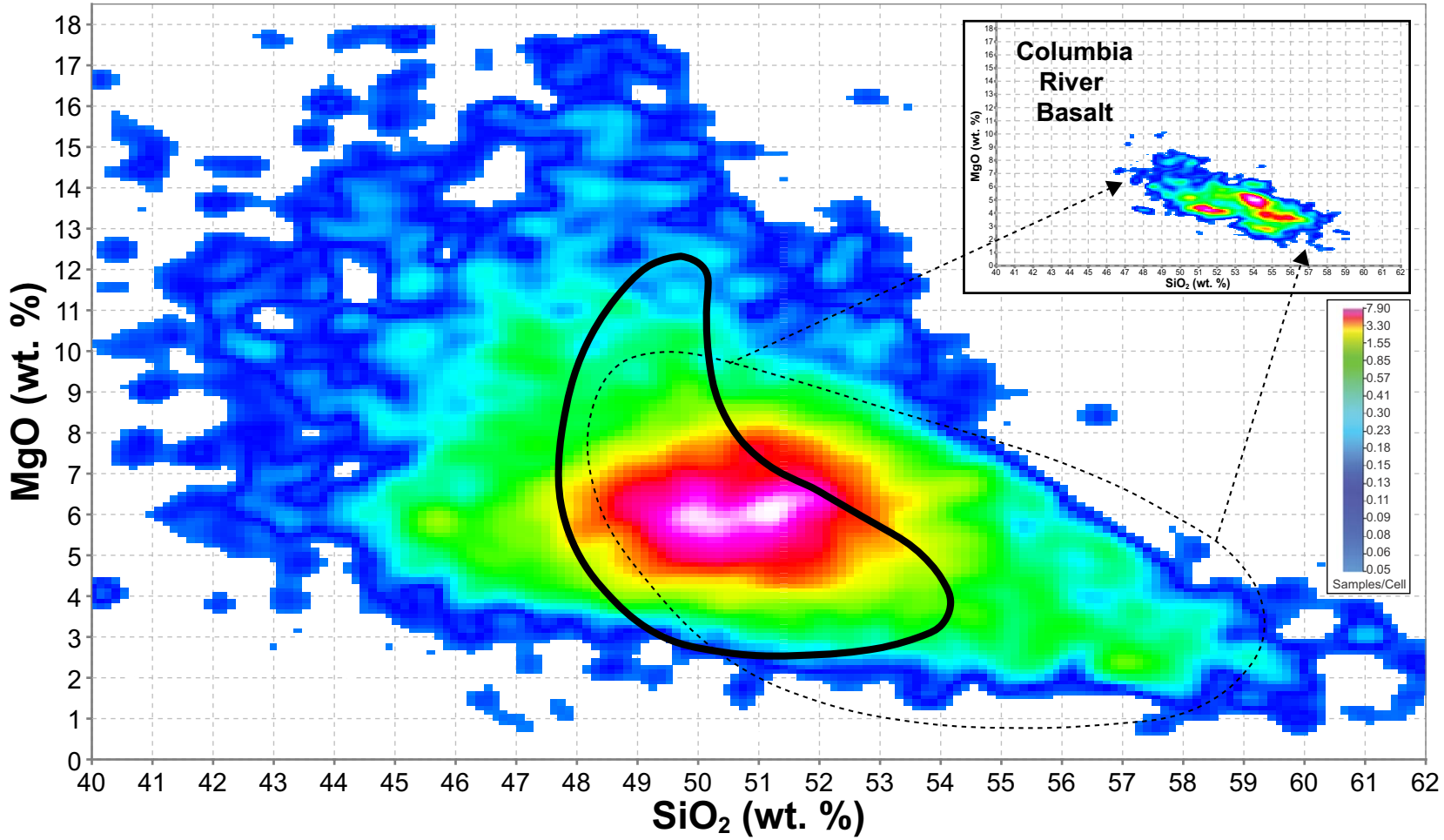

Figure 3. Comparison of MgO versus SiO_2 for continental flood basalts (CFB). Density contours on main figure are the bulk of CFB (Siberian Traps, Deccan Traps, Paraná, Karoo and Ferrar, Emeishan, Central Atlantic Magmatic Province), solid black line encompasses Steens Basalt data, dashed black line represents the field of all other Columbia River Basalt Group (CRBG). Inset shows density contours for all other CRBG. Density contours are color-coded as shown on inset, by number of samples per cell, where each cell is 0.1 wt% on all sides, and warmest colors represent highest sample density. Data from precompiled files of each province are from the GeoRoc database, accessed June 2016.

the upper Steens Basalt is less widespread, with a minimum estimated footprint of ~33,000 km^2 (Camp et al., 2013). Where both are exposed at Steens Mountain, the upper Steens Basalt is approximately two-thirds of the section, making for an upper Steens Basalt volume of ~13,200 km^3, compared to 18,600 km^3 for the lower Steens Basalt.

The Steens Basalt is inferred to have come from a combination of isotopically defined mantle sources including a depleted mid-ocean ridge-like source (C1 source of Carlson, 1984; Pacific mid-ocean ridge basalt of Wolff and Ramos, 2013) and an ocean island basalt type component (Imnaha component of Wolff and Ramos, 2013) or a depleted mantle component that has been contaminated by subducted oceanic sediments (C2 of Carlson, 1984). Potential crustal contamination in the upper Steens Basalt is based on elevated $^{87}Sr/^{86}Sr_i$ (see proximity to $^{87}Sr/^{86}Sr_i$ lines; Fig. 2) and enrichment in incompatible elements (Wolff et al., 2008; Wolff and Ramos, 2013).

Under Steens Mountain, the crust is 32–35 km thick, thins to 30 km west under the adjacent High Lava Plains and northern Basin and Range, and thickens to 42 km to the east, coincident with the $^{87}Sr/^{86}Sr_i$ 0.706 line (Fig. 2) taken to be the edge of the North America craton (Eagar et al., 2011). Steens Mountain lies just west of the $^{87}Sr/^{86}Sr_i$ 0.704 line. The crust of eastern Oregon is made of accreted Paleozoic to Mesozoic terranes stitched with Mesozoic plutons (Walker and MacLeod, 1991). The lower crust is inferred to be mafic and dense with a thin, still denser root, implying substantial intraplating and underplating of the crust by mafic magma (Cox and Keller, 2010; Eagar et al., 2010; Wagner et al., 2010). Carlson and Hart (1987) argued that substantial crustal genesis in the region is through gabbroic intraplating, analogous to Shervais et al. (2006) who suggest abundant fractional crystallization in a series of sills left a seismically imaged 10 km LMI in the crust along the Snake River Plain, located primarily in the state of Idaho, USA. The mantle under Steens Mountain is part of a low-velocity upper mantle anomaly that extends under the High Lava Plains (Oregon, USA) and Snake River Plain (Gao et al., 2011; Wagner et al., 2010; Warren et al., 2008).

ANALYTICAL METHODS

Sampling

A transect of samples was collected at Steens Mountain by Johnson et al. (1998; Fig. 4) and has since been defined as the type section of the Steens Formation, or Steens Basalt (Camp et al., 2013). Samples for this study were

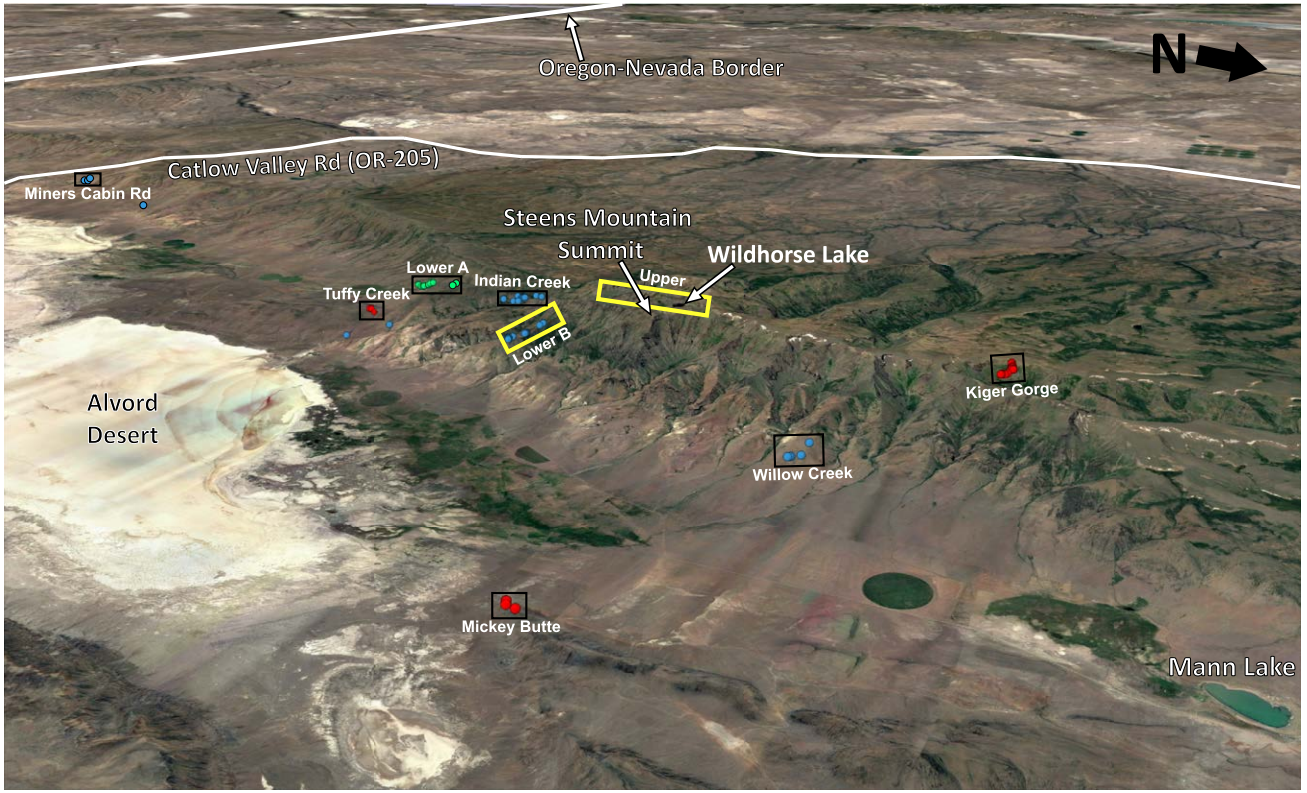

Figure 4. Oblique view of Steens Mountain, from Google Earth looking southwest, showing Steens Basalt sample locations (circles) from this study, color-coded to chemical affinity (green—lower A; blue—lower B; red—upper). Yellow rectangles outline the transect of Johnson et al. (1998), the type section of Steens Basalt. Black rectangles outline additional sections sampled for this study, and detailed in Figure 5. The three solitary blue sample points are from dikes sampled for this study that cross cut basement. North-south distance along the scarp from Mann Lake to the southernmost samples is 55 km.

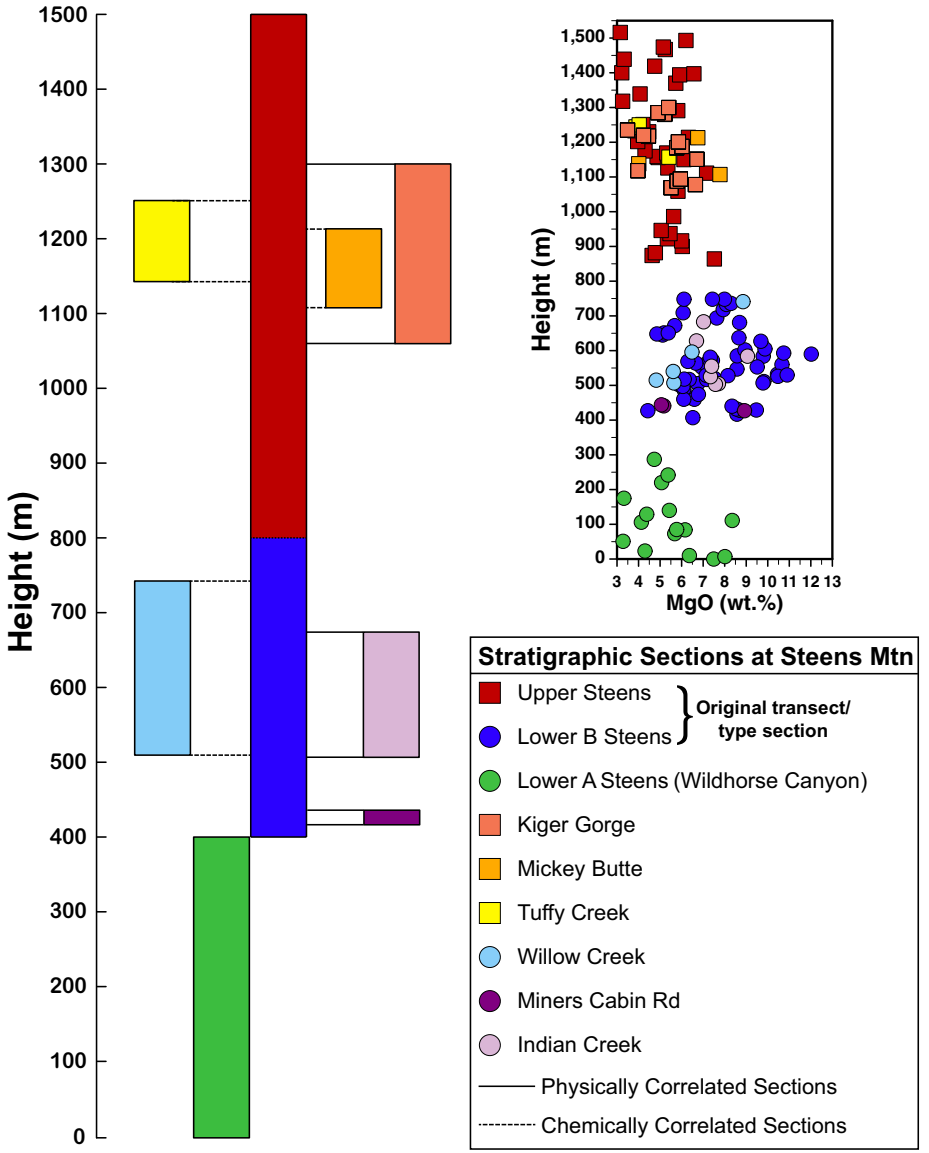

Figure 5. Correlation of new sample sections with the original transect/type section of the Steens Basalt. The original type section at Steens Mountain is shown in blue and red (lower B and upper Steens, respectively). The sections that were both physically and chemically correlated to the type section are shown with solid lines, whereas those that were chemically correlated only have dashed lines. Finer dashed line between lower B and upper Steens Basalt reflects the uncertainty in the location of transition between these two phases. See text for further explanation. Inset of MgO wt% versus stratigraphic height establishes the chemical correlation of these sections that is also evident in many other major and trace elements; see text for discussion.

taken from individually recognized flows and compound flow lobes of greater than 0.5 m where not pervasively altered. Some flows were sampled multiple times where mineral texture variations were evident. We treat each of these samples as separate chemical proxies of the Steens Basalt magmatic system. Between 2013 and 2016, sampling was conducted to replenish samples that were exhausted from original analysis (Johnson et al., 1998) and reanalysis by Wolff et al. (2008). Johnson et al. (1998) originally measured a composite of two sections summing to 982 m, but they acknowledge that a section of flows at the transition was unsampled. We have added 115 m to the transition (gap at ~800 m on inset Fig. 5), but sampling remains incomplete due to poor accessibility. We also sampled additional sections to document lateral variability and to search for the base of the formation. Samples were collected as far north as Willow Creek, as far south as Miners Creek Road, and to the east of Steens Mountain at Mickey Butte (Fig. 4). The Wildhorse Canyon section of the lower Steens Basalt occupies a paleovalley and is ~400 m thick; at least 25 compound flow lobes and sparse single flows are exposed, of which we sampled 18 of the least altered massive interiors. The Wildhorse Canyon section exposes flows that stratigraphically underlie the base of the previously recognized lower Steens Basalt flows. These lowest Steens Basalt flows in Wildhorse Canyon overlie a flow that appears texturally similar to the pre-Steens andesites (ca. 19 Ma, Minor et al., 1987b). We refer to this newly identified lower Steens Mountain section from Wildhorse Canyon as the lower A Steens Basalt section, and to the original lower Steens Basalt as lower B Steens Basalt. Wherever we subsequently refer only to "lower" Steens, this includes both the A and B sections.

Each of the stratigraphic sections sampled for this study have been correlated to the original transect (Fig. 5) by physical correlation, which is based on elevation and location relative to the original transect, and/or by comparing the variation in chemical patterns with stratigraphy in the original transect. Detailed flow by flow lithological correlations are not possible. The sections physically correlated include the lower A Steens Basalt (Wildhorse Canyon), Miners Cabin Road, Indian Creek, and Kiger Gorge (Figs. 4 and 5). Lower A Steens Basalt is on strike with the upper Steens Basalt original transect at the head of Wildhorse Canyon, so the stratigraphy was physically correlated by adjusting for elevation difference in the deeper, lower A section. The base of the Miners Cabin Road section is located ~20 m above a contact between Steens Basalt and the underlying Pike Creek Formation. The Indian Creek section is on strike with the highest portions of the lower B original transect, so the stratigraphy was correlated for that section based on elevation comparison with the original transect, as with the lower A section. Kiger Gorge was sampled for the M.S. thesis of Bendaña (2016) at Central Washington University, Ellensburg, Washington, USA, as a collaborative part of this study. The east rim of Kiger Gorge is on strike with the upper Steens Basalt portion of the original transect, near the summit of Steens Mountain. We took the difference in elevation of the summit sample from the original transect and the high point of the east rim of the gorge to find the stratigraphic height that would correlate with the original section on the east rim. We then accounted for a 5° dip of the Steens Basalt

flows over the 2 km distance from the Kiger Gorge east rim to the west rim, where the section was sampled. By then assigning that stratigraphic height in the section from the east rim to a given elevation on the west rim, we were able to determine a correlating stratigraphic height to each sample in the Kiger Gorge section. All of these sections were also chemically correlated.

The remainder of the sections were correlated with the original transect by comparing compositional changes up section (Mickey Butte, Tuffy Creek, Willow Creek; Figs. 4 and 5) as physical correlations are impossible due to various fault interactions. The inset of Figure 5 shows changes in MgO wt% with stratigraphic height, color-coded to match each newly sampled section. The patterns match closely with their original transect counterparts; trends of increasing or decreasing MgO match over a similar range of height. We do not expect a perfect correlation given the nature of the Steens lava flows (dominantly compound pahoehoe) and potential paleotopography; nevertheless, the chemical patterns are well matched. This holds true for the majority of other elements, including most of the major elements, Ni, Cr, Cu, Rb, Ba, Sr, Nb, Zr, and the rare earth elements (REE) (not shown). None of the physical or chemical correlations suggest that the lower A Steens Basalt is exposed in any of the sections other than in Wildhorse Canyon. The gaps in the chemical section (inset Fig. 5) reflect unsampled regions, mainly owing to inaccessibility, and thus the exact stratigraphic location of transition between lower A, lower B, and upper Steens Basalt is uncertain.

^{40}Ar-^{39}Ar Dating

We selected sample NMSB-55 for ^{40}Ar-^{39}Ar dating as it represents the basal flow from the lower A section and overlies a pre-Steens andesite flow. As this sample is sparsely phyric (<1% plagioclase and olivine), a microcrystalline groundmass separate was analyzed. Hand selected chips were crushed in a disk mill or mortar and pestle, and then sieved to 150–212 µm. A non-magnetic groundmass fraction was separated and acid leached following the procedure of Koppers et al. (2011). About 20 mg of the least altered material was handpicked for analysis. The sample was then irradiated and analyzed at the TRIGA (training, research, isotope, general atomics) nuclear reactor and Argon Geochronology Lab at Oregon State University, Corvallis, Oregon, USA, according to the protocol of Koppers et al. (2011). Irradiation and analytical protocol, all analytical results including total fusion age, normal and inverse isochrons, mean square of the weighted deviates, operating conditions, constant values and other metadata are summarized in Supplemental File 1[1].

Mineral Compositions

Compositions of olivine, clinopyroxene, plagioclase, Fe-Ti oxides, and chromium spinel were obtained using a Cameca SX-100 at the Electron Microprobe Laboratory, College of Earth, Ocean, and Atmospheric Sciences, Oregon State University. Accelerating voltage was set to 15 kV, with a beam current of 30 nA. Beam diameter was set at 1 µm for all phases except plagioclase, which was analyzed at 5 µm. Peak count times ranged from 10 to 60 seconds depending on the phase and element of interest. Smithsonian microbeam standards were used to calibrate for each mineral phase and multiple points of each standard were analyzed as unknowns to determine analytical error. Supplemental File 2 (footnote 1) contains mineral composition data for all phases analyzed from the lower Steens Basalt, as well as calibration standards and error. Mineral phases analyzed from the upper Steens Basalt are reported in the M.S. thesis of Graubard (2016) from Central Washington University.

Major and Trace Element Compositions

Major and trace element analysis was conducted at the P.R. Hooper GeoAnalytical Laboratory at Washington State University (WSU), Pullman, Washington, USA, using a ThermoARL Advant'XP + sequential X-ray fluorescence (XRF) spectrometer and an Agilent 7700 quadrupole inductively coupled plasma–mass spectrometer (ICP-MS). Select rock chips from each sample were ground for 2 min in a tungsten carbide SPEX Shatterbox grinding mill. Powders were fused into beads using a 2:1 mix of dry dilithium tetraborate flux to dry rock powder and placed in graphite crucibles, then heated in a 1000 °C furnace for 10 min. Beads were re-ground in tungsten carbide for 1 min, 1 g of powder was weighed out for ICP-MS analysis, and the remaining powder was re-fused by the above method to ensure sample homogeneity. The resulting bead was used for XRF analysis, and the 1 g aliquot of powder was dissolved and used for ICP-MS analysis. Reproducibility for XRF analyzed elements is less than analytical error (Kelly, 2016). Precision for the ICP-MS method is generally 5% (relative standard deviation) for the REE and 10% for the remaining trace elements. Analytical procedure, accuracy, and precision are described by Johnson et al. (1999) for XRF and by Knaack et al. (1994) for ICP-MS. All XRF and ICP-MS compositional data for the samples obtained for this study, analytical detection limits, and other precision and accuracy details are in Supplemental File 3 (footnote 1).

Weighted Bootstrap Resampling

In order to verify that chemical distinctions between the lower A, lower B, and upper Steens Basalt are statistically significant, the weighted bootstrapping approach was employed, which is a statistical resampling technique. In this approach, values from a data set are randomly sampled to estimate a particular population parameter. In this case, the mean of each element concentration in the whole rock data set was cast from random subpopulations. The Steens Basalt data were divided into lower A, lower B, and upper sets, with a total of 16, 55, and 60 samples in each, respectively. Only samples with a full suite of major, trace, and REE data were selected, which includes all samples

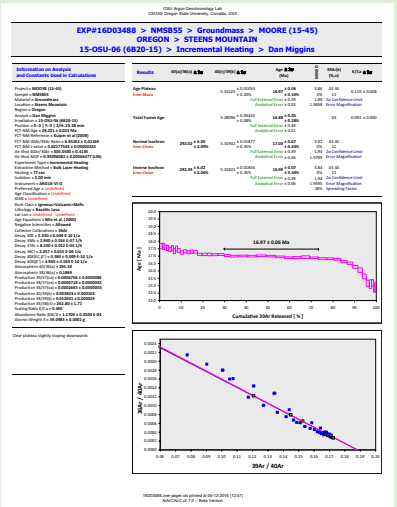

[1]Supplemental Files. File 1: Analytical protocol and full results for Ar-Ar age dating of lower A Steens Basalt basal flow. File 2: Mineral composition data for olivine, clinopyroxene, plagioclase, and Fe-Ti oxides analyzed from the lower Steens Basalt for this study. File 3: Whole-rock major and trace element compositions, analytical precision and accuracy, and sample location details for Steens Basalt samples from this study. File 4: Bootstrapping data sets, calculations and results. File 5: Whole-rock data plots demonstrating a lack of cryptic alteration in Steens Basalt Samples. Please visit https://doi.org/10.1130/GES01665.S1 or access the full-text article on www.gsapubs.org to view the Supplemental Files.

from this study, and the subset of samples from Johnson et al. (1998) that were reanalyzed by Wolff et al. (2008). Samples from dikes were excluded.

The filtered data sets were then used to determine the mean and standard deviation for each element of interest (51 total elements) in each section. Samples were weighted independently in each set to account for some flows that were sampled multiple times (done so to capture within flow heterogeneity), using the following equation:

$$w = 1 - \left(\frac{n_{analyses}}{n_{total}}\right) \Big/ \left(\frac{n_{maximum} + 1}{n_{total}}\right)$$

where $n_{analyses}$ is the number of samples from a given flow, n_{total} is the total number of samples in the section (lower A, lower B, or upper), and $n_{maximum}$ is the number of samples in the largest location (i.e., the most sampled flow in the section). For each data set, the values of each element were randomly sampled 100 times, with replacement of the values after each sampling, to determine a bootstrapped mean and standard deviation. This approach was repeated 50 times, for a total of 50 bootstrapped mean and standard deviation calculations. The bootstrapped mean values were compared to values across the data sets and to the true mean of each set. The selected individual data sets, mean calculations and bootstrap results are reported in Supplemental File 4 (footnote 1).

Ar-Ar AGE FROM LOWER A STEENS BASALT SECTION

The lowest Steens Basalt flow in the lower A section (sample NMSB-55) gives a weighted plateau age of 16.97 ± 0.06 Ma (2σ) and establishes ca. 17 Ma as the onset of CRBG volcanism. The weighted plateau age was calculated from 11 contiguous heating steps that contained ~45% of the total ^{39}Ar released (Fig. 6). Age calibration was performed using the Fish Canyon Tuff sanidine standard age of 28.201 ± 0.023 Ma (1σ; Kuiper et al., 2008). The overall plateau is generally well behaved, though it does contain some typical early excess and late depleted steps, and isochron regression is within error of the 295.5 atmospheric ^{40}Ar/^{36}Ar value (Supplemental File 1 [footnote 1]). This new date is the oldest reported from samples at Steens Mountain, and the oldest high-precision Ar-Ar age of the Steens Basalt (see summary of Steens Basalt Ar-Ar ages by Camp et al., 2013; all recalculated to the Fish Canyon sanidine monitor age of 28.201 Ma of Kuiper et al., 2008 and with 2σ analytical errors), but it is within error of a few lower B Steens Basalt flows that are stratigraphically higher (cf. sample JS-5—16.84 ± 0.43 Ma, Camp et al., 2013).

STEENS BASALT FLOW MORPHOLOGY, TEXTURES, AND PETROGRAPHY

The lower B Steens Basalt package is thickest at Steens Mountain and comprises 35–40 mainly compound flow lobes that are relatively thin (usually 0.5–5 m, as also described in Bondre and Hart, 2008). The upper Steens Basalt includes more single flows and more a'a, and is generally thicker than those of the lower Steens (~5–10 m), but not as thick as typical CRBG (~10–100 m, cf. Long and Wood, 1986; Reidel et al., 2013). The Steens Basalt pahoehoe flows were mainly emplaced by inflation processes (Bondre et al., 2004; Bondre and Hart, 2008; Camp et al., 2013), as were the rest of the much thicker CRBG flows (Self et al., 1996, 2014). Flow tops and bases tend to be vesicular, whereas flow cores are largely non-vesicular and massive with crude columnar to blocky jointing. Diktytaxitic textures are common, as is secondary zeolite mineralization resulting in amygdaloidal textures. Weathering horizons are sometimes present at the contacts between flows or lobes and contain accumulations of red, oxidized sediment, likely from chemical weathering of flow or lobe tops.

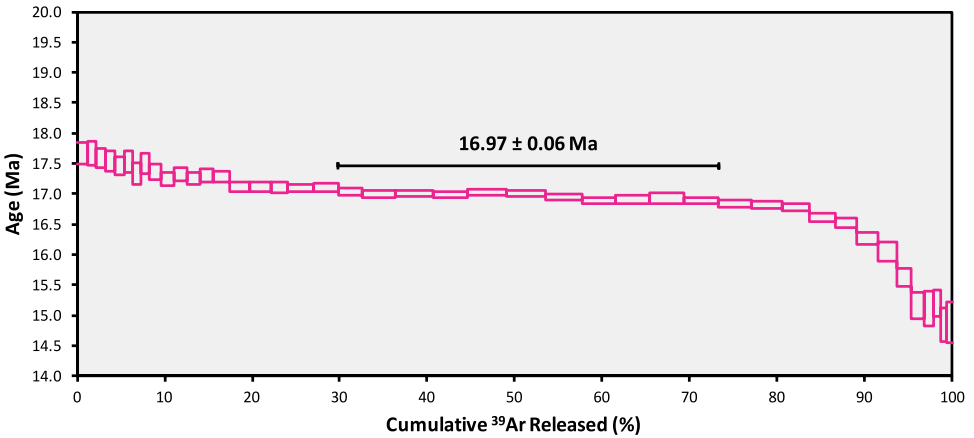

Figure 6. Age spectrum for groundmass Ar-Ar incremental age determination on sample NMSB-55. The weighted plateau age is 16.97 ± 0.06 Ma (error is ±2σ) and was calculated from 11 contiguous heating steps that contained ~45% of the total ^{39}Ar released.

Development of these horizons is moderate in the lower A Steens Basalt, but generally lacking in the lower B Steens Basalt. Weathering horizons become more abundant between flows and lobes in the upper Steens Basalt, particularly in Kiger Gorge, where they are up to a few cm thick and separate almost all of the uppermost flows. Inasmuch as flow or lobe thickness does not vary radically through the section, eruptive frequency is a proxy for effusion rate. The occurrence of weathering horizons early and late, but not in the middle of the section, demonstrates moderate eruptive frequency at the onset of volcanism, followed by high-eruptive frequency, returning to modest frequency near the end of Steens Basalt emplacement.

Textures and modal mineralogy in the Steens Basalt lavas are variable and range from sparsely phyric, to olivine phyric, to plagioclase and olivine phyric, to extremely plagioclase phyric (Fig. 7). The abundance of phyric lavas is in stark contrast to the voluminous basaltic andesite members of the CRBG (Grande Ronde Basalt), where flows are sparsely phyric (cf. Hooper, 1982, 1984; Reidel et al., 1989b; Takahahshi et al., 1998). Textural types vary from lower to upper Steens Basalt (Fig. 7). Lower Steens Basalt flows contain multiple olivine phyric flows (Fig. 7A), and modal olivine is typically 2%–7%; it reaches 15% in rare cases. In the upper Steens Basalt, olivine is scarcer, making up only a few percent, and is only found in tandem with other phenocryst phases. Olivine

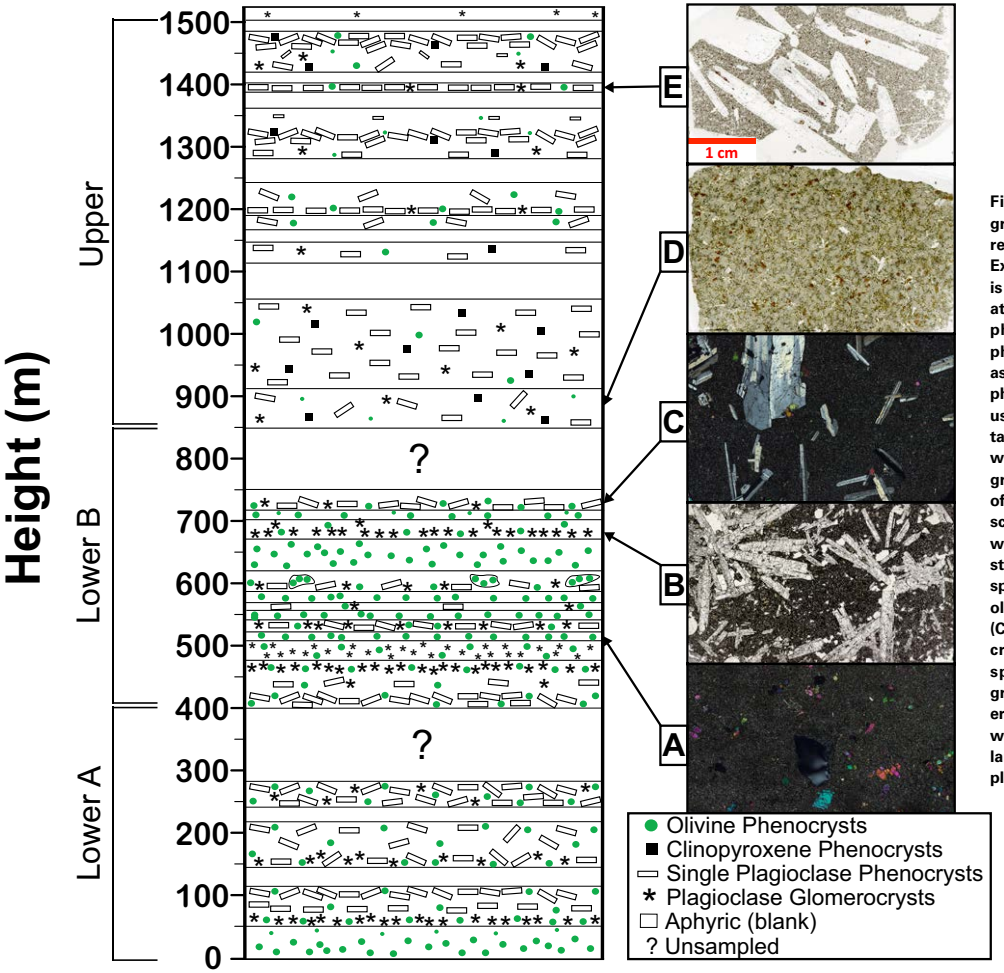

Figure 7. Textural changes with stratigraphic height and photomicrographs of representative Steens Basalt textures. Extent/thickness of each chemical section is shown on the far left. Systematic variations in textural types and phenocryst phases occur up section (e.g., olivine phenocryst phase decreases up section as clinopyroxene appears as a phenocryst phase up section, see text for details). We use the term phenocrysts to denote crystals large enough to see in hand sample, with no genetic implications. Photomicrographs of full thin sections display some of the most common textural types, 1-cm-scale bar applies to all: (A) Olivine phyric with very fine groundmass, (B) daisy stone type plagioclase glomerocrysts with sparse olivine phenocrysts and abundant olivine microphenocrysts between laths, (C) single-isolated type plagioclase phenocrysts with occasional glomerocrysts, sparse olivine, and cryptocrystalline groundmass, (D) single isolated and glomerocrysts of plagioclase microphenocrysts with abundant clinopyroxene, and (E) very large, flow aligned single-isolated type plagioclase with rare olivine.

appears as single microphenocrysts to phenocrysts or in glomerophenocrysts where individual crystals range from 0.5 to 5 mm. Olivine is typically euhedral but commonly has a cracked appearance. Chromium spinel and melt inclusions are often found in olivine grains. Resorption (as embayments or resorbed cores) is occasionally present in the phenocrysts from flows with the greatest range of Fo content (see Mineral Compositions) and is more common in the upper Steens Basalt. Phenocrystic clinopyroxene is rare in the lower Steens Basalt but becomes more abundant in the upper Steens Basalt; subophitic to ophitic textures are common in the lower part of the section, where clinopyroxene is dominantly an anhedral oikocryst phase. Plagioclase is found in several distinct size populations: groundmass microlites, microphenocrysts, phenocrysts, and megaphenocrysts (Table 1). Crystals of all size populations are largely euhedral and frequently contain oxide mineral inclusions as well as melt inclusions. Disequilibrium textures are infrequent in plagioclase from the lower Steens Basalt, but are pervasive in the upper Steens Basalt flows, most commonly as sieve texture. Oxide minerals are common and include magnetite and ilmenite as groundmass phases and as inclusions in plagioclase and clinopyroxene, as well as chromite inclusions in olivine. We have not identified sulfides or apatite in the lower Steens Basalt. Neither zircon nor baddeleyite has been recovered from large samples (M. Coble and S. Burgess, personal commun., 2017).

The Steens Basalt is known for conspicuous giant plagioclase laths (1–5 cm in diameter). Textures in these giant plagioclase basalts (GPB) are variable and

TABLE 1. REPRESENTATIVE LOWER STEENS MINERAL COMPOSITIONS

Sample/Type	Grain_Spot[†]	Grain type[§]	SiO_2	TiO_2	Al_2O_3	FeO*[#]	MnO	MgO	CaO	Na_2O	K_2O	NiO	Cr_2O_3	Total	Fo/Mg#[††]	An[§§]
JS22[##]																
Olivine	2_c	Phenocryst	38.62	0.011	0.061	18.55	0.25	42.19	0.253	0.012	0	0.238	0.036	100.2	80.2	N.A.
Olivine	2_m	Phenocryst	38.95	0.021	0.051	18.44	0.247	42.4	0.258	0.012	0.017	0.266	0.045	100.7	80.4	N.A.
Olivine	2_r	Phenocryst	38.54	0.017	0.078	20.43	0.248	40	0.294	0.004	0.004	0.256	0.041	99.91	77.7	N.A.
Clinopyroxene	2_c	Microphenocryst	50.39	1.432	4.24	9.795	0.009	14.89	18.36	0.395	0	N.A.	0.552	100.1	73.0	N.A.
Clinopyroxene	2_r	Microphenocryst	50.35	1.346	3.004	12.02	0.101	14.32	17.99	0.38	0.014	N.A.	0.042	99.57	68.0	N.A.
Plagioclase	9_c	Phenocryst	48.92	0.057	31.81	0.56	N.A.	0.178	15.44	2.652	0.066	N.A.	N.A.	99.68	N.A.	76.3
Plagioclase	9_m	Phenocryst	49.39	0.068	31.96	0.518	N.A.	0.16	15.16	2.784	0.093	N.A.	N.A.	100.1	N.A.	75.1
Plagioclase	9_r	Phenocryst	49.27	0.069	31.72	0.499	N.A.	0.164	15	2.784	0.082	N.A.	N.A.	99.57	N.A.	74.9
Ilmenite	7_c	Groundmass	0.027	47.45	0.002	48.18	0.526	1.382	0.048	N.A.	N.A.	0	0.029	98.27	N.A.	N.A.
Magnetite	17_c	Groundmass	0.083	24.14	1.623	66.53	0.492	1.938	0.025	N.A.	N.A.	0.048	0.147	96.09	N.A.	N.A.
Chromite	5_c	Inclusion in Ol	0.094	1.571	29.34	31.25	0	11.59	0.023	N.A.	N.A.	0.21	24.28	98.84	N.A.	N.A.
NMSB-13																
Olivine	22_c	Microphenocryst	39.12	0.029	0.048	21.76	0.318	39.21	0.257	0.013	0	0.223	0.031	101	76.3	N.A.
Olivine	22_m	Microphenocryst	38.86	0.015	0.028	21.38	0.316	39.65	0.257	0.018	0.014	0.203	0.025	100.8	76.8	N.A.
Olivine	22_r	Microphenocryst	38.56	0.011	0.035	22.1	0.303	39.01	0.27	0.002	0	0.199	0.028	100.5	75.9	N.A.
Clinopyroxene	3_c	Microphenocryst	49.65	2.052	3.92	12.03	0.223	13.68	18.35	0.392	0.006	N.A.	0.061	100.3	67.0	N.A.
Clinopyroxene	3_r	Microphenocryst	48.43	2.573	4.567	13.91	0.236	13.33	17.19	0.425	0.001	N.A.	0.052	100.7	63.1	N.A.
Plagioclase	10_c	Megaphenocryst	50.8	0.071	31.17	0.613	N.A.	0.136	13.79	3.268	0.168	N.A.	N.A.	100	N.A.	70.0
Plagioclase	10_m	Megaphenocryst	52.11	0.07	30.65	0.597	N.A.	0.137	13.49	3.573	0.191	N.A.	N.A.	100.8	N.A.	67.6
Plagioclase	10_r	Megaphenocryst	51.32	0.072	30.73	0.63	N.A.	0.141	13.63	3.414	0.178	N.A.	N.A.	100.1	N.A.	68.8
NMSB-18																
Olivine	1_c	Phenocryst	39.67	0.011	0.04	16.62	0.221	42.66	0.238	0.012	0.006	0.287	0.05	99.82	82.1	N.A.
Olivine	1_m	Phenocryst	38.33	0.014	0.058	16.87	0.226	42.68	0.242	0.022	0.007	0.282	0.054	98.78	81.8	N.A.
Olivine	1_r	Phenocryst	38.1	0.017	0.032	17.72	0.187	42.1	0.264	0.006	0	0.234	0.037	98.7	80.9	N.A.
Olivine	4_c	Phenocryst	40.06	0.014	0.058	15.14	0.199	43.87	0.238	0.023	0	0.32	0.053	99.98	83.8	N.A.
Olivine	4_m	Phenocryst	39.41	0.013	0.062	15.64	0.208	43.82	0.257	0.009	0.005	0.339	0.057	99.82	83.3	N.A.
Olivine	4_r	Phenocryst	38.45	0.023	0.052	16.45	0.229	43.42	0.248	0.005	0	0.218	0.049	99.14	82.5	N.A.

Note: All mineral chemistry results for each phase analyzed in this study reported in Supplement 1. N.A.—not applicable.
[†]Grain indicates the grain number analyzed from a given sample, spot is the analyzed location on that grain (c—core, m—midpoint, r—rim).
[§]Groundmass grains are <0.5 mm, microphenocrysts are 0.5–1 mm, phenocrysts are 1 mm to 1 cm, megaphenocrysts are >1 cm.
[#]Fe is reported as all FeO*.
[††]Fo—forsterite content of olivine; Mg# (for clinopyroxene only)—$Mg/(Mg+Fe^T)$.
[§§]An—anorthite content of plagioclase.
[##]Original sample from Johnson et al. (1998) (whole rock reported therein), mineral compositions analyzed in this study.
Ol—olivine.

include (1) distinctive radial, snowflake-like plagioclase clusters with olivine trapped at spoke apices (aka "daisy stone" of Annells, 1973; Fig. 7B), and (2) sandwich-structured glomerocrysts of plagioclase laths with microphenocrystic olivine trapped between laths. The latter often contains phenocrystic olivine grains or glomerocrysts that are isolated from the plagioclase clusters. Textures 1 and 2 are pervasive in the lower Steens Basalt (Fig. 7). Another texture of GPB (3) contains single, isolated plagioclase laths with abundant olivine inclusions (Figs. 7C–7E); this type more commonly occurs in the upper Steens Basalt. The megaphenocrysts and glomerocrysts are typically 1 cm, but as large as 5 cm in diameter. GPB laths, whether in glomerocrysts or as single isolated crystals, are euhedral and make up a few percent to more than 50% of the rock. GPB are also described for the Deccan and Emeishan (China) flood basalt provinces (e.g., Higgins and Chandrasekharam, 2007; Talusani, 2012; Cheng et al., 2014; Sheth, 2016), attesting to similar magmatic processes across CFB.

On outcrop scale, GPB erode in a grusy, rounded style that makes them recognizable at a distance. In contrast, sparsely phyric or olivine phyric flows crop out in cliffy vertical ledges with crude columnar to blocky jointing and develop prominent talus slopes. In the lower Steens Basalt, GPB form large packages of compound flow lobes, mostly daisy stone lobes that can be tens to nearly 100 m thick, and these large packages are intercalated with olivine phyric flow lobes a few meters thick (Fig. 7). Internally, the GPB flows commonly transition abruptly to more crystal poor textures, either nearly aphyric or containing much smaller and less abundant plagioclase phenocrysts (0.5–2 cm), usually as very thin lenses that we interpret as flow tops. In the upper Steens Basalt, GPB packages are restricted to tens of meters thick and are dominantly single isolated megaphenocryst type flows (Fig. 7). The GPB flows there are interbedded with flows that lack phenocrysts or contain sparse microphenocrysts of dominantly plagioclase. Textures in the lower A Steens Basalt section are most like those described for lower B Steens Basalt but have some characteristics common to upper Steens Basalt as well. Olivine is slightly less abundant and plagioclase is more often resorbed than in the rest of the lower Steens Basalt. Single isolated type GPB flows occur in the lower A section more frequently than in the lower B Steens Basalt, but glomerocrystic type GPB flows occur more frequently in the lower A than in the upper Steens Basalt.

MINERAL COMPOSITIONS

New detailed mineral chemistry on the lower Steens Basalt reveals cryptic variations in olivine, clinopyroxene, and plagioclase compositions, signaling temporal changes in magmatic conditions (Fig. 8; Table 1; Supplemental File 2 [footnote 1]). These changes up section are analogous to the cryptic layering typical of LMI (see Discussion below) and are also evident in whole rock composition (see Major and Trace Element Compositions). Forsterite (Fo) content is homogeneous from core to rim of olivine in some flows (e.g., $Fo_{79–78}$, $Fo_{83–80}$, $Fo_{84–81}$), but heterogeneous in others (e.g., $Fo_{85–77}$, $Fo_{84–63}$, $Fo_{78–60}$; Fig. 8). Fo range in individual flows does not necessarily correlate with whole rock MgO or Mg# (Mg# = 100*[Mg/(Mg+Fe^T)]); two different flows with >10 wt% MgO and Mg# ~66 have $Fo_{84–67}$ and $Fo_{84–81}$. However, the maximum Fo content in a given flow does correlate with MgO; the higher the whole rock MgO, the higher the maximum Fo. The majority of olivine grains are normally zoned with respect to MgO. Reverse zoning is rare and generally restricted to trace elements (particularly Ni) but is notable in the flows with the most homogeneous forsterite content. Average core Fo is greatest in the lower B section, and is less in the lower A and upper Steens Basalt sections.

Clinopyroxene is dominantly a late stage groundmass phase present as magnesian augite. As with olivine, Mg# can be quite homogeneous in some flows (Mg# 64–67, 62–68), and heterogeneous in others (Mg# 60–78, 61–77; Fig. 8). Typically, but not universally, flows with homogenous olivine compositions also have more restricted ranges of Mg# in clinopyroxene (Fig. 8).

Plagioclase compositions vary modestly within or between flows; the full range of core compositions is $An_{78–58}$ and of rims is $An_{76–43}$. Megaphenocrysts larger than 1 cm in GPB flows are remarkably homogeneous; the core to rim variation in anorthite (An) content is typically less than 10 and can be as little as three. The full range of core compositions from all analyzed megaphenocryst grains is $An_{74–57}$. Phenocrysts (less than 1 cm) and microphenocrysts (larger than 0.5 mm) have a slightly larger compositional variation overall; cores have the full range reported above, and rims range from $An_{74–43}$, with a few exceptions that are $<An_{60}$. The An range within individual flows does not correlate with whole rock Mg# (i.e., flows with both high and low Mg# have similar plagioclase compositional ranges), and the An range of individual flows does not vary significantly with increasing stratigraphic height (Fig. 8).

The extent of compositional heterogeneity tends to correlate across all three mineral phases in the lower Steens Basalt. Flows with restricted compositional ranges in mineral phases alternate with flows characterized by crystals with wider compositional ranges (Fig. 8). Mineral compositions for the upper Steens Basalt (Graubard, 2016) document a change into that part of the section (Fig. 8). Olivine and clinopyroxene become less magnesian and plagioclase ranges to less calcic compositions. The ΔFo or ΔMg# in olivine and clinopyroxene, respectively, do not change significantly from lower to upper Steens Basalt, but plagioclase composition, measured as ΔAn (Fig. 8) becomes more heterogeneous into the upper Steens Basalt.

THERMOBAROMETRY

Olivine-liquid thermometry using olivine and whole rock compositions from the lower Steens Basalt gives a temperature range of 1180–1350 °C for equilibrium samples (Putirka, 2008). None of the few olivine grains analyzed from upper Steens Basalt are in equilibrium with their whole rock compositions. A new clinopyroxene-liquid thermobarometer (Neave and Putirka, 2017) using clinopyroxene and whole rock compositions yields a temperature range of 1170–1190 °C and a pressure range of 3.4–5.6 kbar for lower Steens

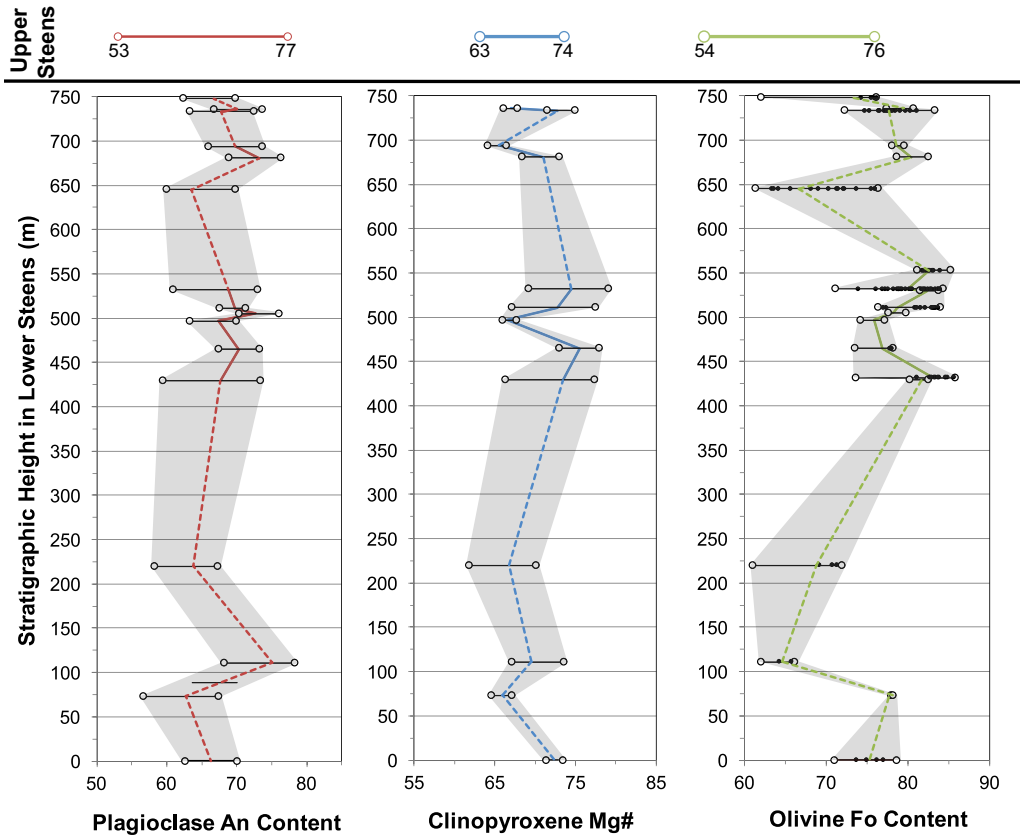

Figure 8. Olivine, clinopyroxene, and plagioclase mineral composition versus stratigraphic height for the lower Steens (lower A and B), in comparison to full ranges for the upper Steens. An—anorthite; Fo—forsterite; Mg#—100*[Mg/(Mg+Fe^T)]. Open circle end caps connected by solid horizontal black lines represent maximum and minimum values from grain core analyses within a sample (flow) at a given stratigraphic height. Colored lines connect mean core compositional values between flows and are solid connecting stratigraphically continuous flows or dashed where all variability between flows is not captured (unsampled or unanalyzed flows). Small black circles in the olivine composition diagram are individual data points for all analyzed cores in the flows with more heterogeneity (not shown for clinopyroxene as that phase is less common and there are few analyses, or for plagioclase because the data are generally evenly spread across the range for that phase). Gray fields to outline the excursions and how the compositional ranges change from analyzed flow to analyzed flow up section. Olivine analyses are limited from the lower A section (four lowest samples) because the flows in that section are typically highly altered. At the top of the figure, the full range of An, Mg#, and Fo content for minerals of the upper Steens (Graubard, 2016) records a change up section to less magnesian olivine and slightly lower Mg# in clinopyroxene, but a similar range of An content.

Basalt equilibrium samples. This same thermobarometer gives a temperature of 1126 °C and 5 kbar for the one clinopyroxene grain in equilibrium with its whole rock sample from all analyzed upper Steens Basalt clinopyroxenes. Oxygen fugacity as estimated from equilibrium Fe-Ti oxide pairs using the ILMAT program (Lepage, 2003) range from QFM to QFM-1 for lower Steens Basalt. Fe-Ti oxides have not been analyzed from the upper Steens Basalt; however, best-fit MELTS and Magma Chamber Simulator (MCS) modeling (Moore et al., 2015; Bendaña, 2016; Graubard, 2016) consistently suggest this same range of oxygen fugacity is appropriate for the upper Steens Basalt samples. The pressure estimates given above have also been further constrained by MELTS and MCS modeling (Moore et al., 2015; Bendaña, 2016; Graubard, 2016); pressures above 4 kbar require orthopyroxene as a liquidus phase, but orthopyroxene is absent in all Steens Basalt samples. Best-fit models from computational modeling of samples from all phases of the Steens Basalt consistently suggest the pressure range is limited to 1–4 kbar for the magmatic system.

MAJOR AND TRACE ELEMENT WHOLE-ROCK COMPOSITIONS

New whole-rock major and trace element analyses clarify the chemical distinctions between lower A, lower B, and upper Steens Basalt, with a zig-zagging pattern of generally less magnesian and more incompatible trace element enriched compositions at the base (lower A Steens Basalt) and the top (upper Steens Basalt) of the section, but more magnesian and incompatible trace element poor flows in the middle (lower B Steens Basalt). These compositional variations, first recognized by a detailed set of whole rock data from a transect of samples by Gunn and Watkins (1970), reflect changes in magma differentiation processes through time as the Steens Basalt evolved. Whole rock compositions presented here include all samples collected for this study (Table 2; Supplemental File 3 [footnote 1]) as well as those samples originally reported by Johnson et al. (1998) and reanalyzed by Wolff et al. (2008), as those samples are from the type section of the Steens Basalt and are the basis for the

TABLE 2. REPRESENTATIVE WHOLE-ROCK MAJOR AND TRACE ELEMENT COMPOSITIONS

Unit	Lower A			Lower B				Upper		
sample	NMSB-55	NMSB-62	NMSB-69	NMSB-5	NMSB-13	NMSB-18	NMSB-21	NMSB-1	NMSB-2	NMSB-4
Major elements (wt%)										
SiO_2	48.14	48.86	48.06	48.66	48.76	47.18	49.96	48.34	52.01	51.72
TiO_2	1.818	1.994	2.744	2.110	1.842	1.752	2.756	2.672	2.623	2.580
Al_2O_3	15.69	16.16	14.61	15.09	18.46	13.42	14.24	15.22	13.38	13.44
FeO*†	11.30	11.27	13.08	11.74	9.90	11.36	12.82	14.36	13.43	13.33
MnO	0.171	0.176	0.200	0.186	0.154	0.183	0.200	0.201	0.214	0.211
MgO	7.36	6.04	5.23	8.53	6.03	10.62	5.34	5.40	3.90	3.96
CaO	9.86	9.02	8.16	9.45	10.63	9.88	9.07	8.59	7.64	7.66
Na_2O	2.90	3.13	3.34	2.88	3.01	2.28	2.97	3.45	3.53	3.30
K_2O	0.66	1.08	1.39	0.74	0.51	0.46	1.40	1.17	1.76	1.74
P_2O_5	0.288	0.365	0.553	0.334	0.250	0.217	0.391	0.418	0.401	0.372
Mg#§	56.3	51.5	44.2	59.0	54.7	64.9	45.2	42.7	36.5	37.0
Total	98.19	98.08	97.36	99.73	99.54	97.36	99.15	99.82	98.89	98.32
LOI%	0.75	1.47	1.40	N.A.	N.A.	N.A.	N.A.	N.A.	N.A.	N.A.
Trace elements by XRF (ppm)										
Ni	150	94	58	233	126	302	63	78	13	16
Cr	221	106	48	554	191	812	118	58	68	75
V	308	315	403	295	294	298	405	420	418	420
Ga	19	20	21	20	21	16	21	22	22	23
Cu	190	140	235	140	135	140	204	318	203	184
Zn	96	103	125	107	88	96	119	134	135	137
Trace elements by ICP-MS (ppm)										
La	11.87	16.36	23.43	16.08	12.00	11.41	21.11	19.96	21.79	20.47
Ce	28.89	37.77	54.97	37.04	27.69	26.67	47.67	44.30	47.99	45.18
Pr	4.19	5.32	7.74	5.27	4.02	3.87	6.77	6.37	7.00	6.55
Nd	19.59	23.74	34.30	23.37	18.10	17.41	30.13	28.73	31.53	28.95
Sm	5.24	5.99	8.56	5.91	4.89	4.69	7.71	7.41	8.11	7.59
Eu	1.83	2.02	2.70	2.02	1.73	1.64	2.50	2.32	2.47	2.38
Gd	5.40	6.21	8.69	6.13	5.15	5.13	8.16	7.62	8.55	7.95
Tb	0.89	1.01	1.38	1.00	0.83	0.85	1.32	1.18	1.40	1.29
Dy	5.41	6.09	8.37	5.92	4.91	5.12	7.95	7.32	8.51	8.00
Ho	1.07	1.22	1.62	1.15	0.97	0.99	1.57	1.45	1.70	1.61
Er	2.77	3.12	4.33	2.91	2.47	2.53	3.97	3.72	4.42	4.16
Tm	0.38	0.43	0.59	0.41	0.34	0.35	0.56	0.52	0.62	0.59
Yb	2.28	2.70	3.57	2.37	2.01	2.06	3.25	3.15	3.74	3.58
Lu	0.34	0.41	0.54	0.38	0.30	0.31	0.51	0.49	0.56	0.54
Ba	238	393	491	289	210	178	397	470	580	597
Th	0.97	2.01	2.55	1.80	1.13	1.41	3.00	2.56	3.72	3.60
Nb	7.42	9.14	12.85	10.73	7.85	7.63	12.47	10.06	10.91	10.60
Y	26.34	30.14	40.87	28.68	24.02	24.37	38.72	35.80	42.55	39.79
Hf	3.24	4.01	5.54	3.93	3.25	3.32	5.26	4.98	5.58	5.33
Ta	0.48	0.61	0.85	0.72	0.53	0.52	0.87	0.68	0.75	0.72
U	0.34	0.69	0.83	0.40	0.24	0.27	0.93	0.75	1.42	1.33
Pb	2.37	4.02	5.55	3.20	2.17	2.26	4.94	5.16	7.43	7.18
Rb	10.6	18.4	23.4	9.4	6.4	7.8	25.5	18.2	36.9	37.1
Cs	0.36	0.21	0.33	0.17	0.10	0.11	0.59	0.26	1.25	1.28
Sr	481	462	448	427	510	325	395	474	366	373
Sc	30.6	29.1	32.7	28.4	24.0	30.7	32.4	31.9	39.8	40.4
Zr	119	151	210	154	123	126	203	191	211	203

Note: All whole-rock compositions obtained in this study reported in Supplement 3. XRF—X-ray fluorescence; ICP-MS—inductively coupled plasma–mass spectrometry; LOI—loss on ignition; N.A.—not applicable.

†Fe is reported as all FeO*.

§Mg#—Mg/(Mg+Fe^T), Fe^T is calculated as 0.90 FeO*.

stratigraphic context of all samples for this study. They are the only other existing samples with a full suite of major and trace element chemistry (major, minor, trace, and all REE—all conducted by XRF or ICP-MS at WSU). Also presented is whole rock chemistry from Kiger Gorge, a section in the upper Steens Basalt, from the M.S. thesis of Bendaña (2016). There is no evidence for cryptic alteration by anoxic waters, as described for the Sentinel Bluffs Member of the Grande Ronde Basalt (Supplemental File 5 [footnote 1]; Sawlan, 2017).

The difference in major element composition between the lower and upper Steens Basalt is evident in the total alkalis versus silica diagram (Fig. 9). All of the samples plot in or near the field that encompasses the data of Camp et al. (2013), a large set of XRF analyzed samples from multiple sections located across the entire region of Steens Basalt exposure. The majority of the lower B Steens Basalt samples are subalkaline and tholeiitic, whereas the bulk of upper Steens Basalt samples plot just into the alkaline field and are a combination of basalt, trachybasalt, and more evolved basaltic trachy-andesite. This mildly alkaline trend is atypical of the other main phase units comprising the CRBG, particularly for the subalkaline Imnaha and Grande Ronde Basalts (as noted by Camp et al., 2013). Lower A Steens Basalt samples straddle the boundary between alkaline and subalkaline fields, and plot mainly as basalt or trachybasalt. Based on CIPW norms, lower Steens Basalts are olivine tholeiites, whereas the upper Steens Basalt is olivine tholeiites and quartz tholeiites; none are nepheline normative. The dikes sampled in the lower Steens Basalt section have compositional affinities mainly with the upper Steens Basalt flows, consistent with the predominant field relationship where dikes cut the lower or upper Steens Basalt stratigraphy. One dike of lower Steens Basalt affinity cuts the local basement (Pike Creek Formation). Early alkalic and picritic magmatism typical of other CFB (cf. Deccan, Karoo [South Africa], Paraná/Etendeka [South America and southwest Africa, respectively]) is lacking in the CRBG, although the lower A Steens Basalt contains some flows that are transitional to mildly alkalic.

Diagrams comparing compositional variation with stratigraphic height further emphasize the distinctions between the lower and upper Steens Basalt (Fig. 10A). The eruptive record begins with relatively magnesian compositions in the lower A (~6–8 wt% MgO), with a range in that section from 3 to 8.5 wt%. The MgO range increases and reaches concentrations as high as 12 wt% in the lower B section, and this range is bracketed by two trends, at high and low MgO, toward increasing MgO early in the section, then becoming less systematic higher in the section (blue bars in Fig. 10B). Although there may be modest olivine accumulation in some flows, those with the highest MgO do not have the highest modal abundances of olivine; one flow with 15% olivine has 9.5 wt% MgO (NMSB-19; see Supplemental File 3 [footnote 1]). High in the lower B section, the high MgO range decreases whereas the low range increases (Fig. 10B); eruptions then become less magnesian in the upper Steens Basalt (~3–8 wt%, Fig. 10A). Silica range is moderate in the lower A section (~47–52 wt%), becomes more restricted in the lower B Steens Basalt (~48–51 wt%), and reaches the highest values and widest range in the upper Steens Basalt (~48–54.5 wt%). Incompatible elements (e.g., Rb, Ba) behave similarly, in that the values are lowest and the range most restricted in the lower B Steens Basalt. Incompatible elements are initially heterogeneous/variable in the lower A flows but become more homogeneous up section (Fig. 10A). The upper Steens Basalt lavas have the highest incompatible trace element values and largest ranges.

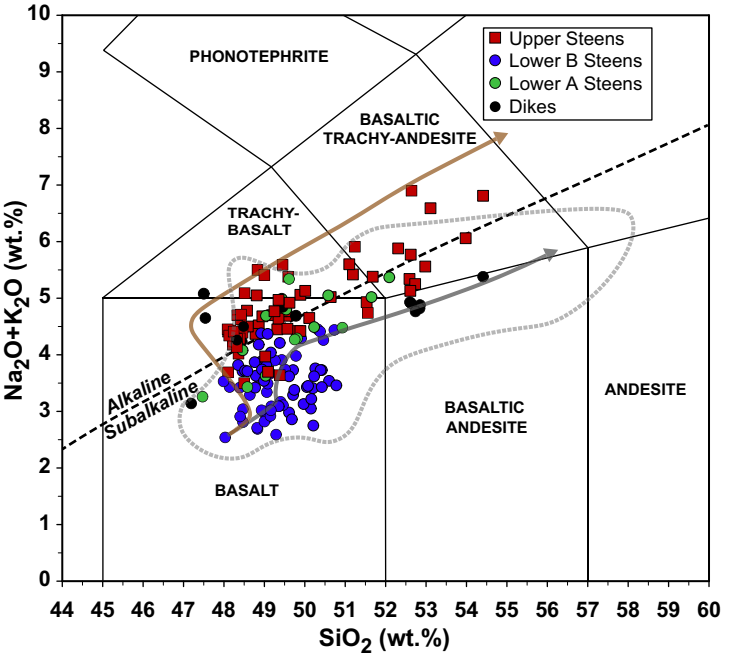

Figure 9. Total alkalis versus silica discrimination diagram. Lower B Steens, is dominantly subalkaline basalt, whereas upper Steens also contains alkaline basalt, trachybasalt, and basaltic trachy-andesite. The lower A Steens flows overlap with both lower B and upper Steens. Dikes tend to have upper Steens compositional affinity, consistent with field relations in which dikes dominantly cross cut lower or upper Steens stratigraphy. Light gray dashed line is the data field of Camp et al. (2013), a large set of X-ray fluorescence analyzed samples across the entire region of Steens Basalt exposure (beyond Steens Mountain). Dark gray and brown transparent lines represent crystal fractionation trends at 1 and 4 kbar, respectively, using the MELTS program (Gualda et al., 2012) and 0.5 wt% H_2O in the parent magma. Data from this study, Johnson et al. (1998) and Wolff et al. (2008) are shown. Upper Steens data includes a new transect from Kiger Gorge (Bendaña, 2016). Alkaline versus subalkaline boundary from Irvine and Baragar (1971).

Weighted bootstrap analysis confirms the distinctions in compositional types from the lower A, lower B, and upper Steens Basalt. Compared to lower A and upper Steens Basalt, true and bootstrapped mean values of the lower B section are distinct in most major and trace elements presented, with the exception of Al_2O_3 (Fig. 11). The lower A section tends to fall either between the lower B and upper Steens Basalt fields (CaO, Na_2O, Sr, Eu/Eu*) or slightly overlap with the upper Steens Basalt (MgO, FeO*, Rb, REE). There is a clear distinction between the REE true means and bootstrapped values of the lower B and

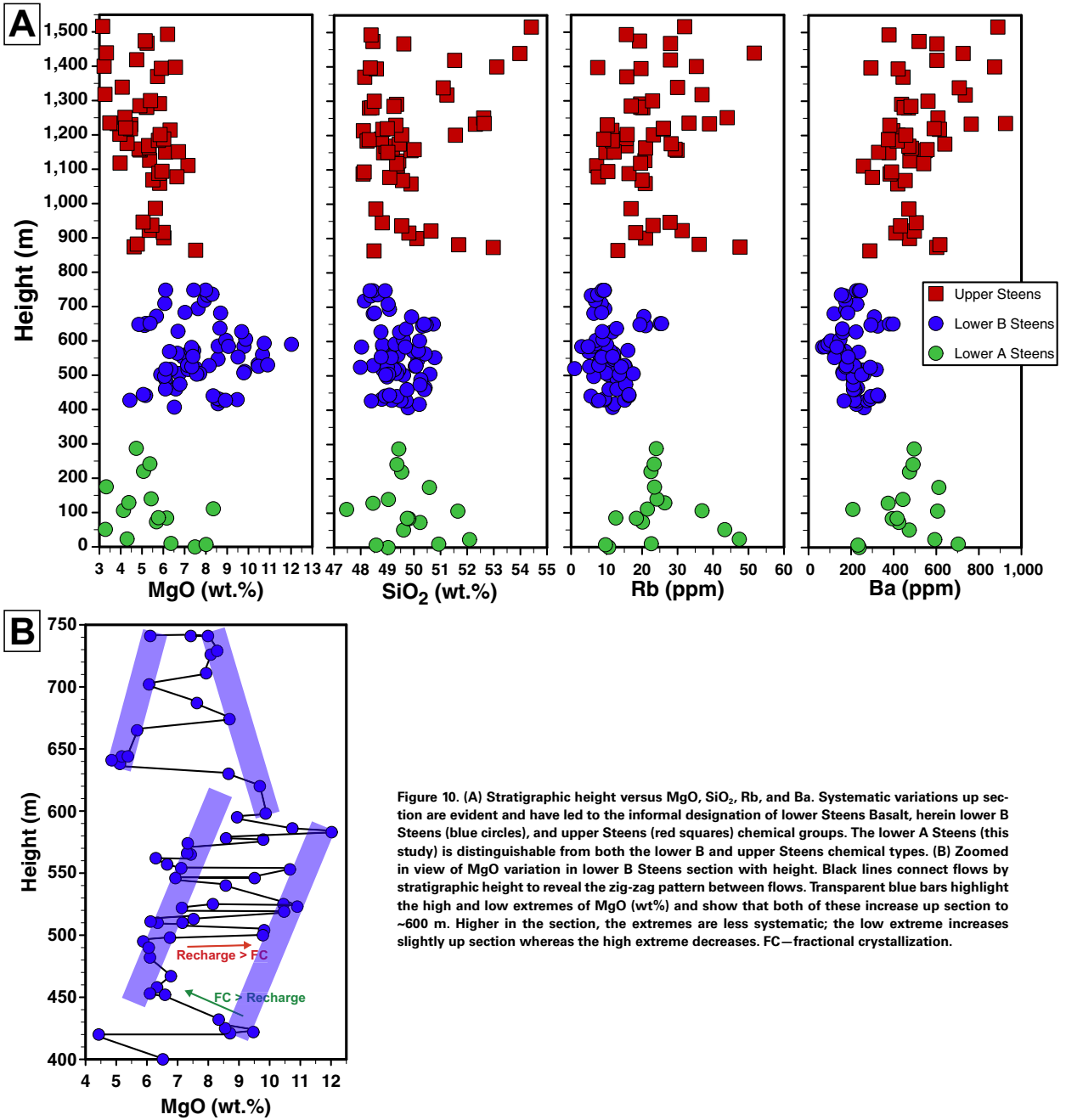

Figure 10. (A) Stratigraphic height versus MgO, SiO_2, Rb, and Ba. Systematic variations up section are evident and have led to the informal designation of lower Steens Basalt, herein lower B Steens (blue circles), and upper Steens (red squares) chemical groups. The lower A Steens (this study) is distinguishable from both the lower B and upper Steens chemical types. (B) Zoomed in view of MgO variation in lower B Steens section with height. Black lines connect flows by stratigraphic height to reveal the zig-zag pattern between flows. Transparent blue bars highlight the high and low extremes of MgO (wt%) and show that both of these increase up section to ~600 m. Higher in the section, the extremes are less systematic; the low extreme increases slightly up section whereas the high extreme decreases. FC—fractional crystallization.

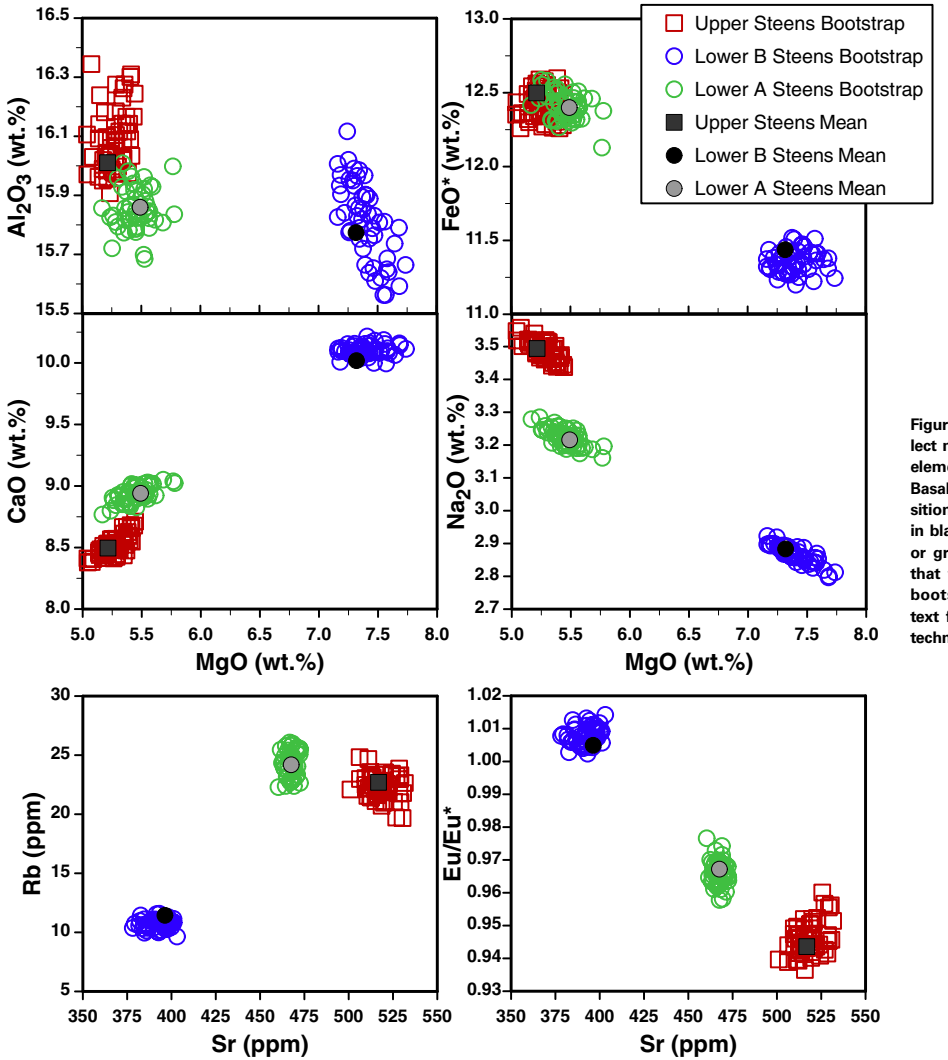

Figure 11. Bootstrapped mean values for select major elements versus MgO and trace elements versus Sr from the three Steens Basalt subgroups. The mean of the compositional data from each subgroup is shown in black (upper—squares, lower B—circles) or gray (lower A—circles) to demonstrate that these values are consistent with the bootstrap calculated mean values. See text for a discussion of the bootstrapping technique.

lower A/upper Steens Basalt, but there is overlap between the REE true means and bootstrapped values of lower A and upper Steens Basalt, particularly in the heavy REE (Fig. 12). The true means of the lower A and upper Steens Basalt REE data fall in the center of the bootstrapped values for each, respectively. The lower B true mean is much lower and distinct from those of the lower A and upper Steens Basalt, and is also on the high end of the bootstrapped values for that group.

Camp et al. (2013) used Ba versus Cr to distinguish between compositional types from the Steens Mountain type section, in order to use these subtypes to categorize a wide range of Steens Basalt samples from across the entire region of exposure. Three subgroups are defined: lower Steens tholeiitic, upper Steens transitional to mildly alkalic, and upper Steens alkalic (Fig. 13). Although there is some slight overlap among fields, the data from this study generally correlate with these fields for the lower B and upper Steens Basalt

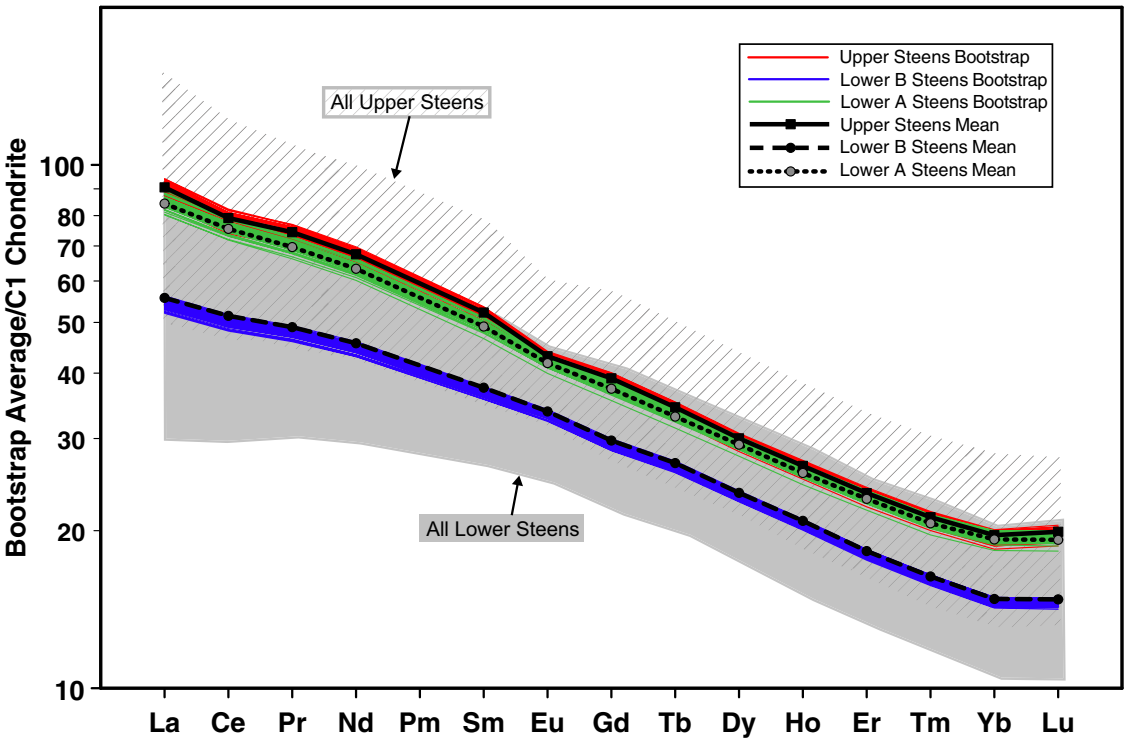

Figure 12. Chondrite normalized rare earth elements (REE) diagram of all analyzed Steens Basalt and bootstrapped mean values from the Steens subgroups. Gray field outlines the full range of lower Steens REE compositions, patterned field with diagonal lines encompasses the full range of upper Steens REE compositions.

samples. Samples from the lower A section plot in all three fields, though the majority plot in the upper Steens transitional to mildly alkalic field, demonstrating the variable character of these initial basalt pulses.

Previous workers have used P_2O_5 versus TiO_2 to distinguish different flows of the CRBG (Hooper, 1982; Hooper et al., 2002; Camp et al., 2003; Reidel et al., 2013), as the flows tend to fall in distinct fields. Camp et al. (2003) noted that the lower B and upper Steens Basalt have two distinct, sub-parallel and slightly overlapping trends (Fig. 14). The fields for the Imnaha and Grande Ronde Basalt flows correlate well to samples of lower B and upper Steens Basalt, respectively, and encompass the majority of the data from the Steens Basalt. Lower B Steens Basalt lavas have Imnaha Basalt like character, whereas lower A and upper Steens Basalt flows generally have Grande Ronde Basalt like character with respect to P_2O_5 versus TiO_2. Thus, we interpret lower B and upper Steens Basalt to be chemically similar to the Imnaha and Grande Ronde formations, respectively. However, some samples of the lower A section straddle the boundary of the Imnaha and Grande Ronde Basalt fields, and one sample plots within the Imnaha Basalt field. Thus, lower A Steens Basalt shares characteristics with lower B and upper Steens Basalt as well as Imnaha and Grande Ronde Basalts.

Collectively, these data support previous interpretations that the Steens Basalt divides into distinct sections; lower B and upper Steens Basalts have been previously divided, and in this study we report a new section, lower A, that shares characteristics of lower B and upper Steens Basalts but may be geographically restricted to a paleovalley in the Steens Mountain source region.

DISCUSSION

Here, we explore temporal changes in voluminous mafic provinces using stratigraphically controlled whole rock and mineral chemical data, beginning with the Steens Basalt. We compare the Steens Basalt history to those of the Imnaha and Grande Ronde Basalts of the CRBG, and to temporal variations in the Deccan and Siberian Traps. Finally, we compare Steens Basalt chemical patterns to those in LMI. The emphasis is on early stages of magmatism during which the plumbing is established to support abundant and frequent eruption of mafic lava.

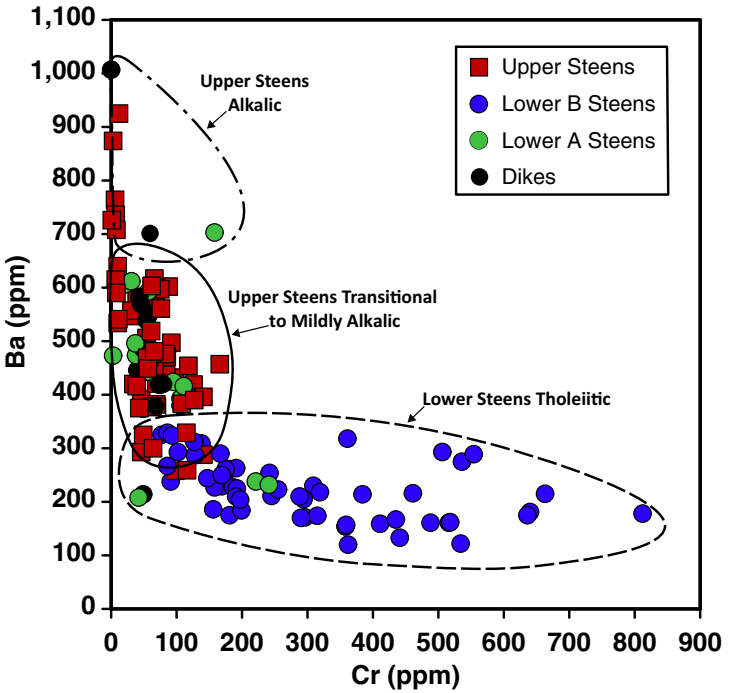

Figure 13. Ba versus Cr as a discriminant between lower and upper Steens Basalt, after Camp et al. (2013). All lower B Steens samples from this study fall within the Lower Steens Tholeiitic field, whereas the lower A Steens and upper Steens samples fall in all three fields.

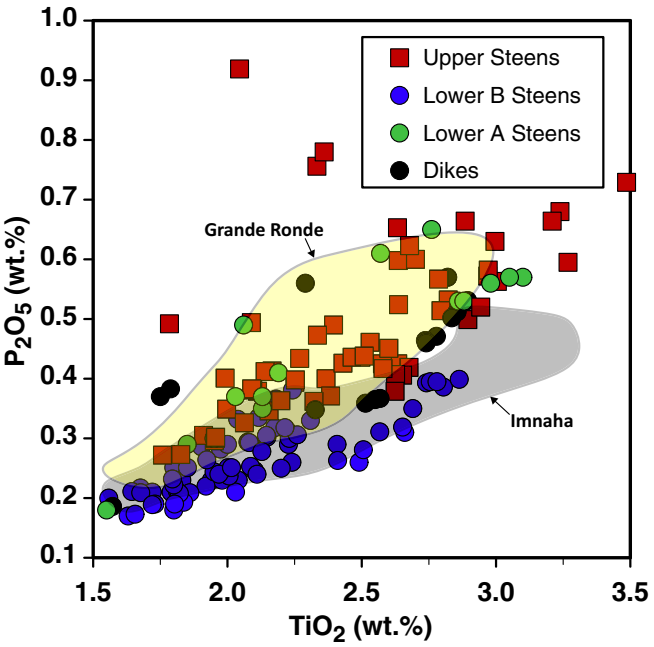

Figure 14. P_2O_5 versus TiO_2 for the lower A, lower B, and upper Steens subgroups and dikes. Gray and yellow fields outline data from the Imnaha and Grande Ronde flows of the Columbia River Basalt Group (CRBG), respectively. Imnaha and Grande Ronde compositional data from a precompiled file of CRBG chemistry in the GeoRoc database (accessed January 2017).

Steens Magmatic Stages

Based on dominant physical and chemical characteristics of each section, the stack of Steens Basalt lavas at Steens Mountain records three distinct stages of magmatism: lower A, lower B, and upper Steens Basalts. The first stage, represented by lower A Steens Basalt, we interpret as an early stage of initially heterogeneous and differentiated magma, signaling early fitful magma ascent, storage, and eruption, and culminating in a magma reservoir capable of delivery of relatively homogenous magma (highest flows in the lower A section, Fig. 10A). At this stage, we suggest that the initial thermal state of the crust is relatively cool, magmas stall and crystallize; relatively evolved compositions therefore erupt. Modest development of weathering horizons between flows speaks to a slower eruption rate than during eruption of lower B Steens Basalt. Diversity of lava textures (Fig. 7) and compositions that overlap the ranges of lower B and upper Steens Basalt sections (Figs. 9–14) indicate variable degrees of differentiation and diverse processes acting during this early stage. Toward the top of lower A Steens Basalt, lava composition is more homogeneous and suggests that a magmatic system capable of erupting relatively homogeneous magma compositions has been established.

The lower B Steens Basalt section lacks weathering horizons, indicating a rapid eruption rate during this time. The section is more mafic overall, with highest MgO and lowest incompatible trace element concentrations (Figs. 10–13) and textures dominated by olivine phyric and glomerocrystic GPB flows (Fig. 7). Mineral chemistry varies up section through the entirety of lower Steens Basalt, from flows with chemically homogeneous phases alternating with flows of heterogeneous mineral compositions (Fig. 8). The overall compositional pattern trends to more mafic compositions early in the section (increasing MgO at both high and low ends, highlighted by blue bars in Fig. 10B), indicating basalt input to the magma system at a rate faster than differentiation, and then a sweep to less mafic compositions, as the rate of basalt recharge compared to fractionation apparently declines. This general pattern up section is overlain by a zig-zag trend between flows from low to high MgO compositions (black lines connecting flows stratigraphically in Fig. 10B), where

the excursion range averages ~4–6 wt% MgO between high and low ends. The sweep to higher MgO signals that initially, recharge outpaces fractionation, and then fractionation outpaces recharge higher (Fig. 10B) in the lower B section. Gunn and Watkins (1970) and Camp et al. (2013) also concluded that fractionation and recharge were important processes in the generation of the Steens Basalt.

The upper Steens Basalt records a general change to more evolved compositions, albeit with numerous excursions between more and less mafic compositions, signaling a continued but comparatively lesser role of mafic recharge. The lower estimated volume of the upper Steens Basalt, along with development of weathering horizons especially high in the section, support the idea of a waning magma system. A decrease in olivine, an increase in clinopyroxene, and a higher frequency of the single isolated plagioclase phyric type of GPB (Fig. 7) further indicate a change in magmatic regime. The slightly larger average flow thickness in the upper Steens Basalt (5–10 m versus <5 m in the lower Steens) likely reflects the increased silica in the upper Steens Basalt (Fig. 10), and hence higher viscosity of the magma.

The upper Steens Basalts lie on a tholeiitic differentiation trend dominated by crystal fractionation and lesser recharge, leading to Fe-rich mildly alkaline, and incompatible element enriched compositions (Fig. 9; Camp et al., 2013; cf. Streck and Grunder, 2012). There is also evidence for an additional role of crustal assimilation in the upper Steens Basalt demonstrated through energy constrained and Magma Chamber Simulator modeling (Bendaña et al., 2017; Graubard, 2016), incompatible trace element ratios and whole rock $^{87}Sr/^{86}Sr$ (Camp et al., 2013; Wolff and Ramos, 2013), and Sr isotopic variations in plagioclase (Ramos et al., 2013). Although a subduction component can mimic crustal contamination, the correlation of increasing Sr isotopic ratios with differentiation indices (decreasing MgO and increasing incompatible elements) lead us to agree with these authors that the trends in the upper section are mainly acquired in the crust. The mineral equilibration pressures for lower and upper Steens Basalt are 1–4 kbar, though abundant shallow crustal staging may mask a deeper history.

Mineral composition also lends insight into the changing nature of the Steens Basalt magmatic system. There are systematic variations of mineral composition, such as correlation between flow MgO and highest Fo in olivine consistent with the overall compositional changes in the lavas. On the other hand, the *range* in mineral composition may be wide or restricted regardless of bulk composition. Variability of olivine composition within single flows is greatest in the lower B Steens Basalt and least in the upper Steens Basalt (largest within flow core range in upper Steens Basalt is $Fo_{76–68,}$ though most flows have cores that vary less than 1 Fo unit; Graubard, 2016). We interpret the variability in the lower B stage to reflect the high rate of recharge, where more primitive basalt repeatedly mixes into resident magma, disturbing the crystallization of equilibrium assemblages. The eruption rate outpaces magma equilibration, leading to more heterogeneous crystal populations. In contrast, during eruption of the upper Steens Basalt, magma has time to equilibrate and is less frequently disturbed by mixing in of recharged magma.

Within each of these stages in the Steens Basalt, a "perched" magma system is established, whereby the system evolves to a characteristic composition after perturbations by recharge, mixing, and/or assimilation. In the lower A section, the magma perches at ~5 wt% MgO high in the section, after a period that produces heterogeneity where compositions range from 3 to 8 wt% MgO (Fig. 10A). In lavas of the lower B section up to 600 m, MgO oscillates between low and high values (ΔMgO = 4–5 wt%), and each "endmember" becomes more magnesian up section (blue bars in Fig. 10B). Excursions to lower MgO suggest that olivine fractionation outpaces recharge, whereas excursions to higher MgO signal episodes of recharge. The system at this stage is dominated by recharge, based on the overall increase in MgO for compositions on both ends of the oscillation. Interestingly, the lower MgO, fractionated lavas are more common, suggesting they are from a more readily tapped, possibly shallower reservoir. In lower B above ~600 m, the range in oscillation declines up section, converging to a narrow range (ΔMgO = ~2 wt%). In the upper Steens Basalt, compositions are generally less magnesian. Early moderate heterogeneity in MgO is followed by more restricted compositions (950–1050 m), followed again by moderate heterogeneity (ΔMgO = ~4 wt%). The least mafic end decreases to ~3 wt% MgO, implying an increased role for crystal fractionation and/or assimilation of wall rock; the latter we propose was facilitated by thermal priming of the crust during earlier stages. An increased role for assimilation/fractional crystallization and less input from recharge is supported by upper Steens Basalt flows having the highest concentrations of incompatible trace elements (Figs. 10–13).

In order to compare the temporal evolution between various CFB and the Steens Basalt, we draw on temporal changes in geochemical data from the CRBG, Deccan Traps, and Siberian Traps, as well as from LMI (Figs. 15 and 16). The objective is to compare within suite variation across provinces. The purpose is not to distinguish mantle sources amongst LIP, but rather to tease out commonalities in differentiation processes in time.

Detailed chemostratigraphic comparisons are readily available for LMI; the characteristic layering in these suites has encouraged many workers to study mineral composition, modal, and phase changes with stratigraphy. On the other hand, for many CFB, samples are grouped by geochemical magma types rather than stratigraphically. Because flow-by-flow stratigraphic reconstructions are rare, the following comparisons to other CFB are generalized.

Comparison to Other Large Mafic Systems—Columbia River Basalt Group

Bryan et al. (2010) describe four endmember types of CFB magma petrogenesis, two that are manifested by large volume basaltic eruptions: type A, which is dominated by olivine phyric lavas with primitive mantle chemical signatures and essentially no crustal staging or contamination; and type B that has a chemical signature reflective of crustal staging, fractional crystallization and mixing, and assimilation at various levels within the crust. The Steens

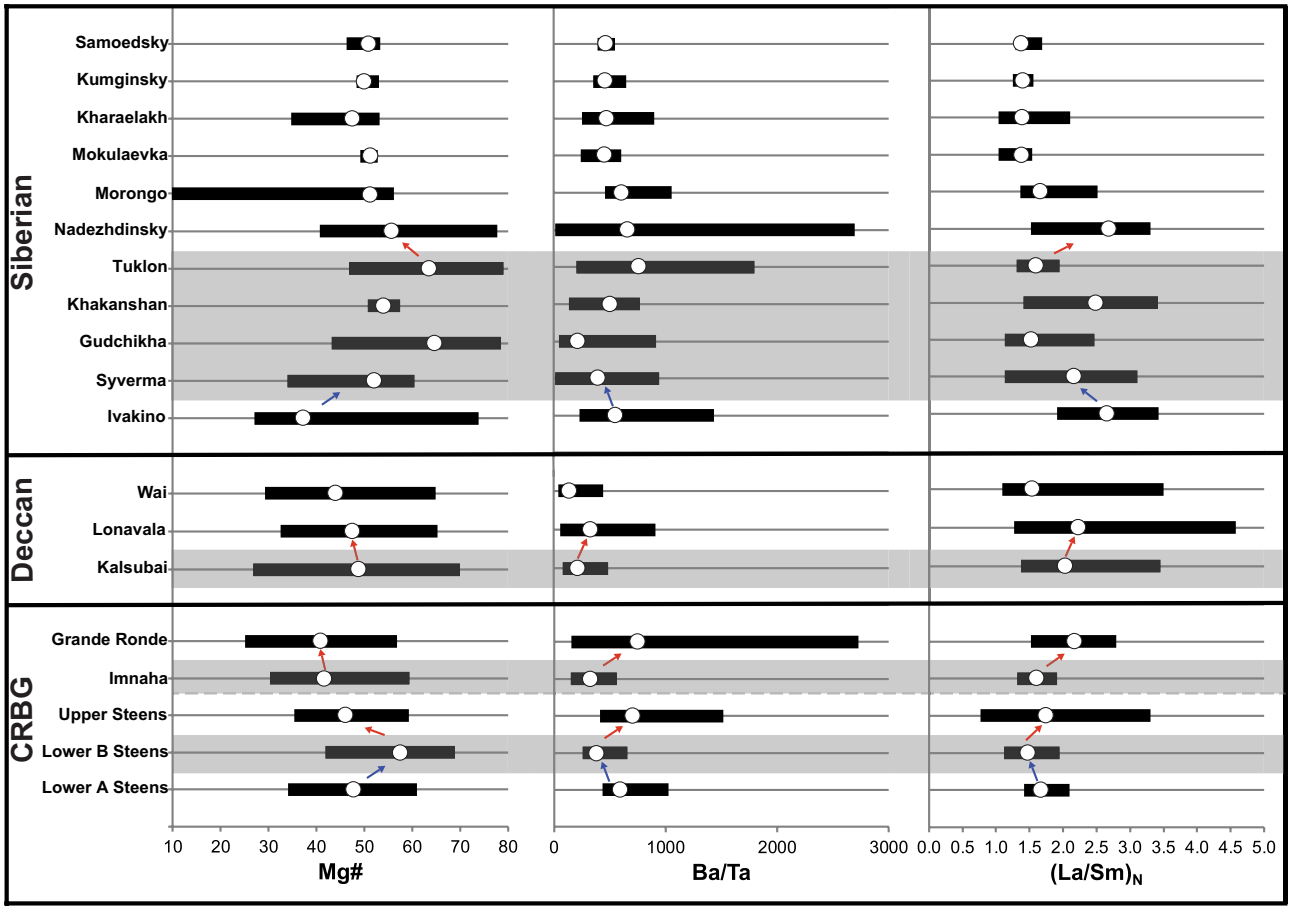

Figure 15. Temporal evolution of whole rock Mg#, Ba/Ta, and $(La/Sm)_N$ for the Columbia River Basalt Group (CRBG), Deccan Traps, and Siberian Traps. Black bars represent the full range of values from each formation or subgroup; white circles represent the mean of each data range. Gray shaded regions highlight sections of each continental flood basalt (CFB) where a mafic, recharge phase is evident. The individual CFB are ordered from most voluminous at the top (Siberian Traps), to least voluminous at the bottom (Steens Basalt). Formations are ordered stratigraphically within each CFB; the dashed gray line at the base of the Imnaha Basalt denotes a transition to the northward section of the CRBG. Blue arrows indicate a shift to a mafic compositional range within CFB (similar to the lower A-lower B Steens transition), whereas red arrows highlight a shift to more evolved compositional ranges (similar to the lower B-upper Steens transition). Imnaha Basalt, Grande Ronde Basalt, Deccan Traps, and Siberian Traps data from GeoRoc precompiled files (accessed June 2016 and January 2017). Mg#—100*[Mg/(Mg+Fe^T)].

Basalt, and the CRBG as a whole, represents the type B endmember, having compositions that range from primitive basalts to more evolved basaltic andesites and signatures that suggest a range of differentiation processes modified the lavas.

Textural and geochemical changes with stratigraphy have also been noted for the Imnaha and Grande Ronde Basalt flows of the CRBG (Wolff and Ramos, 2013). The Imnaha Basalt is coeval with the upper Steens Basalt flows and erupted a total volume of 11,000 km^3 (Reidel et al., 2013), whereas the Grande Ronde Basalt erupted a total volume of 150,400 km^3 (Reidel and Tolan, 2013) after the cessation of Steens Basalt volcanism. Dikes related to the Imnaha Basalt and the Grande Ronde Basalt flows erupted from the Chief Joseph Swarm north of the Steens Basalt dike locus and are more proximal to the North American Craton (Fig. 2). Imnaha and Grande Ronde Basalt flows are significantly thicker than the Steens Basalt flows and lobes, with an average of ~30 m, but

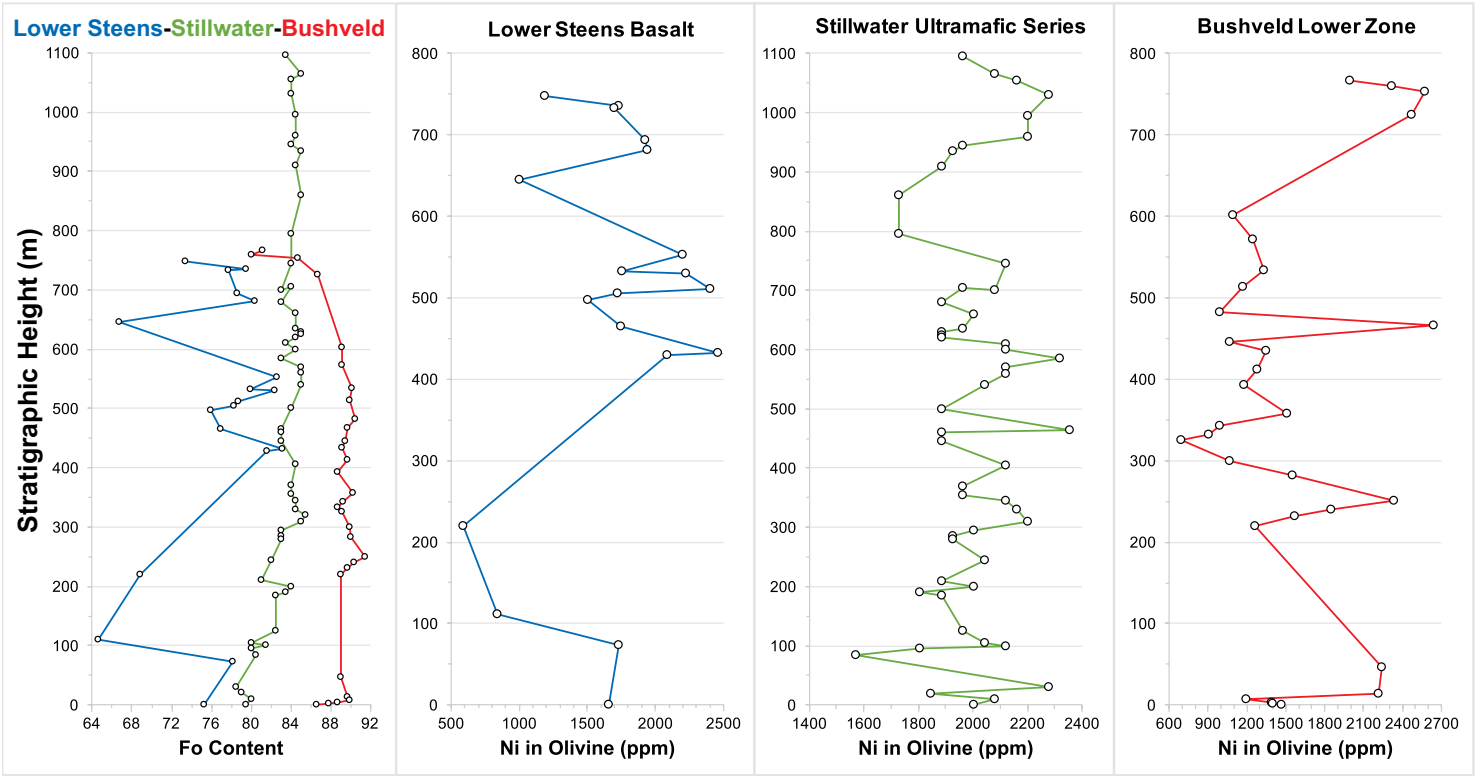

Figure 16. Changes in forsterite (Fo) and nickel (Ni) content (ppm) of olivine with stratigraphic height in the Steens Basalt, Stillwater Complex Ultramafic Series, and Bushveld Lower Zone. Colored lines are coded blue for lower Steens, green for Stillwater, red for Bushveld. For the lower Steens and Bushveld, colored lines connect average Fo content at a given stratigraphic height, and open circles emphasize the location of these averages. For the Stillwater, the line and open circles represent one olivine composition at each given height from a section analyzed by Raedeke and McCallum (1984). In the nickel content panels, the same symbology is followed, but instead each location has a separate panel. Note that the scales vary for both stratigraphic height and nickel content in each location. Bushveld data from the Turfspruit Section Lower Zone of Yudovskaya et al. (2013).

up to ~100 m (Hooper et al., 1984; Reidel and Tolan, 2013). The maximum total thickness of these units is ~3 km, occurring in the Pasco Basin of Washington, USA; the average total thickness is ~1 km (Reidel and Tolan, 2013; Reidel et al., 2013). Imnaha flows are medium- to coarse-grained, with sparse olivine or clinopyroxene phenocrysts, and commonly plagioclase-phyric, including many GPB flows (Hooper et al., 1984; Hooper, 1988). The Grande Ronde flows range from virtually aphyric to sparsely phyric to microphyric, with a groundmass of plagioclase and clinopyroxene (Reidel and Tolan, 2013 and references therein). Imnaha Basalt compositions are comparable to the lower Steens Basalt, although the Imnaha Basalt is generally less primitive than the lower B Steens Basalt (cf. lower Mg# range, Fig. 15). The Imnaha Basalt is divided into two chemical types by Hooper et al. (1984); the lower American Bar flows with slightly more evolved compositions (average SiO_2 = 51.5 wt%, average MgO = 4.8 wt%, and average Mg# 39), and the upper Rock Creek flows with slightly more mafic compositions (average SiO_2 = 49.7 wt%, average MgO = 5.5 wt%, and average Mg# 44). The lowest American Bar flows transition to the lower Rock Creek flows, and then the flows of each chemical type become interbedded upsection (Hooper et al., 1984). This strengthens similarity to lower Steens Basalt, with a lower subunit (lower A Steens Basalt and American Bar) extending to more evolved compositions below a more mafic sequence (lower B Steens Basalt and Rock Creek). As not all Imnaha Basalt data are categorized as either America Bar or Rock Creek types, we do not distinguish these in Figure 15. Grande Ronde Basalt compositions overlap with the upper Steens Basalt (Figs. 14 and 15), but are even more strongly differentiated, as the Grande Ronde Basalt compositions are almost exclusively basaltic andesite. Grande Ronde Basalt follows a subalkaline trend on a total

alkali-silica diagram (Hooper et al., 2002; Camp et al., 2013) as opposed to the slightly alkaline trend of upper Steens Basalt; significant crustal contamination, as proposed for the Grande Ronde Basalt (Camp et al., 2013; Wolff and Ramos, 2013; Ramos et al., 2013), would drive differentiation to calc-alkalinity (Grove et al., 2003; Streck and Grunder, 2012).

The changes up section from Imnaha to Grande Ronde Basalts are analogous to the Steens Basalt stratigraphic evolution in that fractionation and a stronger contribution of crustal contamination are likely responsible for the shift in composition between the basaltic Imnaha and the more evolved Grande Ronde flows, particularly given the availability of the cratonic crust as a potential contaminant for the Grande Ronde Basalt (Carlson et al., 1981; Carlson, 1984; Wolff et al., 2008; Wolff and Ramos, 2013). This is evident in the lower range of Mg#, coupled with generally higher and more variable Ba/Ta and La/Sm_N in the upper Steens and Grande Ronde Basalts compared with their counterparts, the lower B and Imnaha Basalt, respectively (Fig. 15). Effectively, we suggest that part of the differentiation cycle of the Steens Basalt is repeated in a more northerly location. The Imnaha and Grande Ronde Basalt flows ascended and erupted through different basement rocks, and the mantle source ascribed to the Imnaha and Grande Ronde Basalts contains less of a depleted component (Carlson et al., 1981; Carlson, 1984; Wolff et al., 2008; Wolff and Ramos, 2013). Nevertheless, a similar within suite chemical pattern emerges, where the early phase of mafic activity is dominated by recharge without crustal contamination (Imnaha Basalt). This phase is the staging of the mafic magmatic system in the crust that heats the crust and leads to crustal contamination of subsequent basalts (Grande Ronde Basalt).

Eruptive flux makes for an important distinction between the Steens Basalt and the Imnaha-Grande Ronde Basalt events. The recharge-dominated, lower B Steens Basalt corresponds to the time of maximum eruption rate and largest erupted volume. In contrast, the mafic recharge dominated Imnaha Basalt stage produced flows far less voluminous than the overlying Grande Ronde Basalt (~1:14 Imnaha to Grande Ronde, compared to ~1.5:1 for lower to upper Steens Basalt). We attribute the difference to persistence of basaltic input as well as crustal modulation. Together, Imnaha and Grande Ronde volcanism lasted from ca. 600,000 yr to as long as 1 m.y. (Baksi, 2013; Barry et al., 2013), or two to three times the span of the Steens Basalt event. In the Steens Basalt scenario, the initial CRBG pulse impinges on a cold and somewhat refractory crust of accreted oceanic terranes. The mantle input persists long enough to establish a shallow magma reservoir through abundant and rapid basaltic recharge, as evidenced by lower B Steens Basalt compositions. As the mantle flux moves northward (e.g., Camp and Ross, 2004; Jordan et al., 2004; Wolff and Ramos, 2013), eruption rate wanes and produces the fractionation dominated upper Steens Basalt phase, with crustal assimilation owing to thermal priming of a relatively refractory crust. Concurrently, a new locus is established where extensive basaltic injection and recharge produces the Imnaha Basalt that is similar in volume to lower Steens Basalt (11,000 km^3 and 18,600 km^3, respectively). Persistent basalt flux from the mantle heats the more fertile craton-margin crust, which induces crustal assimilation and produces the voluminous Grande Ronde Basalt. High-mass rates of assimilation, greatly exceeding crystallization, can be sustained as wet, alkali-rich partial melts of the crust are added to basalt and lower the liquidus (Reiners et al., 1995), producing crystal-poor basaltic andesite magmas. Although recharge persists, the chemical signature is integrated with crustal assimilation and fractionation processes during the growth of large magma reservoirs capable of erupting the vast volumes of individual Grande Ronde Basalts (flows ≥ 10,000 km^3; Reidel and Tolan, 2013).

Regional rhyolite volcanism associated with the CRBG has been recently recognized (Coble and Mahood, 2012; Benson and Mahood, 2016; Benson et al., 2017; Streck et al., 2015, 2016). It begins after the earliest Steens Basalt eruptions (16.69 Ma near McDermitt Caldera; Henry et al., 2017) and continues until at least 15 Ma. This suggests an important role for crustal staging and assimilation in the CRBG. Felsic magmatism is also associated with other CFB, including the Deccan Traps and the Paraná/Etendeka Traps (Lightfoot et al., 1987; Peate, 1997). Rhyolites of the Rooiberg Volcanics are associated with the Bushveld LMI (Twist and French, 1983).

Comparison to Other Large Mafic Systems—Deccan Traps

Other CFB also display systematic variations in time (Fig. 15). The Deccan Traps in India, a CFB that was erupted from ca. 66.5–65.5 Ma (Renne et al., 2015), have an estimated original volume of 2×10^6 km^3 (Courtillot and Renne, 2003) and a maximum total thickness of 3.6 km (Richards et al., 2015). The Deccan chemostratigraphy is best established for the Western Ghats region that is divided into three major subgroups: the Kalsubai, Lonavala, and Wai (oldest to youngest). Each subgroup is divided into several formations (Beane et al., 1986; Subbarao and Hooper, 1988). Though the Deccan is dominantly composed of aphyric to sparsely phyric flows of olivine ± clinopyroxene ± plagioclase (Beane et al., 1986), GPB are abundant in the Kalsubai; they appear at intervals and define the tops of each individual formation in that subgroup (Beane et al., 1986; Higgins and Chandrasekharam, 2007; Sheth, 2016). Picrites appear throughout the section but are most common in the Kalsubai (Beane et al., 1986). The Deccan Traps share some chemostratigraphic characteristics with the Steens Basalt.

Deccan Trap analogs to Steens Basalt are most evident when considering bulk whole rock compositional changes in stratigraphy. A decrease in maximum and mean Mg# occurs from the Kalsubai to the Lonavala subgroups, but then maximum Mg# stays consistent from the Lonavala into the Wai subgroup, albeit with a larger overall range in the Wai subgroup (Fig. 15). Ba/Ta and La/Sm_N increase in their maximum values, mean values, and ranges from the Kalsubai to the Lonavala, but then decrease in maximum, mean, and range into the Wai (Fig.15). This is distinct from the Steens Basalt in that the highest maximum, mean, and range for these trace elements are found high in the section, in the upper Steens Basalt (Fig. 15). Deccan whole rock compositional changes up section between the Kalsubai and Lonavala are similar to the transitions between lower B-upper Steens Basalt and Imnaha-Grande Ronde

Basalt (red arrows, Fig. 15). Much like the lower B Steens Basalt, we suggest the initial heterogeneity and more mafic compositions in the Kalsubai can be explained by a combination of alternating fractionation and recharge, where recharge generally outpaces fractionation. As with the upper Steens Basalt, we suggest that the Lonavala whole rock compositional characteristics can be explained by fractionation punctuated by periods of magma equilibration with increasing contributions from the crust. The apparent lack of an equivalent of a lower A Steens Basalt section in the Deccan stratigraphy could be because the necessary stratigraphic detail is not sufficiently exposed or has not been sampled. Regardless, the importance of the comparison to the Steens Basalt lies in the suggestion that there is an early, more mafic, recharge-dominated stage during which the system becomes well established in the crust, followed by a period of eruption of more evolved lavas that reflect fractionation and crustal assimilation overprinting mafic recharge.

The Steens Basalt whole rock compositional analog does not extend to the Wai Subgroup. The return to a more tholeiitic nature in this latest Deccan subgroup (Fig. 15; more homogeneous and lower incompatible trace element ratios but similar Mg# range as Lonavala) is distinctive from the shift to a more evolved nature in the latest stages of the Steens Basalt. This likely reflects some fundamental difference in the generation of the final and largest Deccan subgroup. Recent estimates suggest that the Wai represents ~70% of the total volume of the Deccan (Richards et al., 2015). The large volumes in the Wai were fed mainly by inflated sheet flows, in contrast to the dominance of compound pahoehoe flows and rare a'a flows in the Kalsubai and Lonavala subgroups (Bondre et al., 2004; Brown et al., 2011). In this way, the Wai is similar to the most voluminous Grande Ronde phase of the CRBG that also contains enormous inflated flows. The increased volume in the Wai compared to earlier subgroups implies an increase in magmatic flux in this latest stage of Deccan Traps eruptions. Recent models suggest a difference in the process generating the Wai Subgroup compared to its earlier counterparts (Renne et al., 2015; Richards et al., 2015).

Comparison to Other Large Mafic Systems—Siberian Traps

The great Siberian Traps (Fig. 1) may contain a three-stage petrogenetic evolution similar to the Steens Basalt, albeit manifested at a grand scale (estimated original volume >3 × 10^6 km^3; Courtillot and Renne, 2003). This CFB erupted between ca. 252 and 248 Ma (Reichow et al., 2009), but the bulk may have erupted in less than 1 m.y. (Burgess and Bowring, 2015; Burgess et al., 2017). The thickest and most voluminous section is found in the Noril'sk region, where individual, mainly simple flows range in thickness from 1 to 100 m. Textures are aphyric to glomeroporphyritic and the mineral assemblage includes plagioclase ± clinopyroxene ± olivine. Plagioclase dominates the phenocrystic and glomerophenocrystic lavas, comprising typically 5%–10% but rarely up to 20%–30% of the volume. Olivine is found most abundantly in picrites that occur mainly in some of the early formations (Gudchika through Nadezhdinsky, Fig. 15; Fedorenko et al., 1996).

Whole rock compositional data (Fig. 15) for the 11 formations of the Noril'sk region show a similar up section trend (Sharma, 1997). The base formation is evolved, with average Mg# 37 and relatively low La/Sm_N. The next four formations become more mafic (blue arrows, gray shaded region in Fig. 15) and oscillate between an average Mg# of 52–65 with a corresponding overall decrease in average La/Sm_N. The final six formations become slightly more evolved and relatively homogeneous (red arrows, Fig. 15). After a transitional stage, represented by the Nadezhdinsky Formation, this section has a range of average Mg# from 48 to 51, and becomes restricted in average Ba/Ta and La/Sm_N ranges as well. Based on these limited geochemical comparisons, the base formation might represent the first variable pulses of magma with initially heterogeneous and differentiated compositions, similar to lower A Steens. The more mafic formations immediately up section (Syverma through Tuklon, Fig. 15) record a recharge dominant phase, where production of the most mafic lavas occurs due to recharge outpacing fractionation. The oscillations between high and low Mg# "endmembers" among those four formations are similar to the within phase oscillations of MgO in the lower B Steens Basalt. Finally, the uppermost and thickest sequence of slightly more evolved formations represents the fractionation and crustal contamination dominated stage that occurs once the system is well established and becomes capable of delivering relatively homogeneous compositions.

Summary of Comparisons to Other CFB

The broad comparisons we have made between the Steens Basalt and other CFB suggest that there are comparable petrogenetic phases in these systems, although each province has unique characteristics as well. There is evidence in each, regardless of overall volume, for an earlier recharge dominant stage that produces the most mafic compositions (gray shaded regions in Fig. 15) during the waxing pulse of magmatic flux. This is generally followed by a period during which more evolved compositions erupt, once the system is well established (transitions indicated by red arrows, Fig.15). This period of evolved magmatism can be due to fractionation outpacing recharge, abundant crustal assimilation, or both, depending on the persistence and intensity of continued heat input. This general correlation is further supported by the stratigraphic change in MgO of the Mamainse Point Formation from the Keweenawan Flood Basalt Province, in Ontario, Canada, where MgO maximum and range are highest early in the section, then decrease and become more homogeneous up section (Klewin and Berg, 1991). Though a range of volumes is represented by the CFB presented here (Fig. 1), it appears that a similar evolution of dominant crustal processes occurs in time over the life of CFB provinces.

Comparison to Other Large Mafic Systems—Layered Mafic Intrusions

LMI are complementary to CFB and LIP in that they represent the crystallized and cumulate residua that remains in the crust after fractionation of voluminous mafic magmatism. They have a lower olivine-dominated, layered

peridotite section (cf. Stillwater, Bushveld) that is interpreted as evidence of an early stage of frequent mafic recharge (Wager and Brown, 1967; McBirney and Noyes, 1979; Raedeke and McCallum, 1984). These ultramafic sections are overlain by a plagioclase phyric dominant volume, typically recognized mainly as products of abundant and prolonged fractionation (Wager and Brown, 1967; McCallum et al., 1980; Eales et al., 1986). The Bushveld and Stillwater LMI also contain fine-grained dikes, sills, and marginal group rocks of norite, gabbro, and gabbronorite thought to represent the earliest pulses of magmatism, predating the layered series. These earliest pulses may be analogous to the lower A Steens Basalt and earliest Imnaha Basalt (American Bar) in that they include evolved compositions. Stillwater sills and dikes range from 45.8 to 51.7 wt% SiO_2 and 4.1–14.0 wt% MgO (Helz, 1985) and the Bushveld range from 48.1 to 57.0 wt% SiO_2 and 6.8–14.1 wt% MgO (Wager and Brown, 1967; Barnes et al., 2010), bearing in mind that parental liquid compositions of LMI are more magnesian at given SiO_2 than Phanerozoic flood basalts. The olivine phyric, ultramafic portions of the Bushveld and Stillwater LMI represent approximately one-fourth to one-fifth of the total thickness (Wager and Brown, 1967; McCallum et al., 1980; Raedeke and McCallum, 1984); this is comparable to the approximately one-third proportion of lower B to upper Steens Basalt. Pressure estimates of crystallization for the Stillwater and Bushveld are restricted to shallow regimes, in the range of 1.5–3 kbar (Cawthorn and Davies, 1983; Helz, 1995), comparable to the 1–4 kbar pressure estimates for the Steens Basalt (see thermobarometry).

A characteristic of major LMI are the zig-zag patterns in cryptic layering, such as Fo and Ni in olivine, taken to reflect recharge events (Wager and Brown, 1967; McBirney and Noyes, 1979). We compare changes in Fo content and nickel in olivine up section through the lower Steens Basalt (A and B), the Stillwater Ultramafic Series (Raedeke and McCallum, 1984), and the Bushveld Lower Zone (Yudovskaya et al., 2013) in Figure 16. Excursions in Fo content through the lower Steens Basalt are much more pronounced (Fo average range: 82–62) than in the Stillwater (Fo range: 84–78) or Bushveld (Fo average range: 92–80) olivine phyric zones. Olivine Ni excursions in the lower Steens Basalt mirror the excursions in average Fo content, and similar excursions can be seen in the Ni content of olivine in the two LMI; that is, from one stratigraphic unit to the next, dramatic changes in Ni are observed. Olivine Ni characteristics are similar in the lower Steens Basalt and Bushveld: the full range of Ni is similar (2500–500 ppm and 2700–600 ppm, respectively), as is the magnitude of the excursions, or the overall change from one stratigraphic height (lava flow or cumulus layer) to the next, viz., a maximum of ~1500 ppm in both (Fig. 16). These large fluctuations in mineral composition, particularly in Ni content in olivine, record alternating recharge and fractionation processes up section, where the excursions to high Fo or Ni signal periods where recharge outpaces fractionation.

The comparisons we make between phases of the CRBG are mirrored in the LMI. The most striking commonality is the shallow staging of voluminous basaltic melt with a most mafic recharge dominated phase of activity that heralds the dominant volume. The ultramafic portions of LMI represent this recharge dominant stage. When recharge becomes subordinate to fractionation and the crust is thermally primed, a more evolved stage produces the plagioclase phyric dominant volume of LMI. The large volumes of cumulates generated by extensive crystal fractionation over the life of these voluminous basaltic events remakes the crust by mafic intraplating.

Attempts to quantify the intrusive to extrusive proportions for either LMI, CFB, and oceanic LIP are few, but comparisons may illuminate fundamental crustal processes. Cawthorn and Walraven (1998) estimate the Bushveld Complex volume at 3.7–6.0 × 10^5 km^3 and use this estimate in a thermal cooling and crystallization model to determine the volumes of magma erupted. They arrive at a total magma volume of 7.4 × 10^5–1.2 × 10^6 km^3, suggesting the intrusive to extrusive (I:E) ratio is ~1:1, which seems a lower limit. In contrast, for the Ontong Java Plateau, which is an oceanic LIP, an I:E ratio of ~6:1 is implied by estimates of extrusive and total volume (6 × 10^6 km^3 and 4.44 × 10^7 km^3, respectively; Courtillot and Renne, 2003). These I:E ratios suggest that ~50%–85% of the volume of the basaltic pulse of LIP remains behind in the crust. Inasmuch as CFB intersect a lower density crust, the intrusive proportion could be even greater, perhaps explaining why Phanerozoic CFB are typically ~10 times less voluminous than their oceanic counterparts (Fig. 1). It is important to quantify intrusive volumes in CFB to determine if mantle flux is similar in both continental and oceanic LIP. The large potential intrusive volume for these settings would not only render the crust more mafic but may require delamination of deep ultramafic cumulates to maintain a crustal mass balance. Future work will serve to quantify the intrusive to extrusive ratios for the Steens Basalt by estimating volumes of cumulates left in the crust through mass and energy constrained computational modeling using appropriate parental melt compositions.

CONCLUSIONS

The stratigraphic compositional changes of the Steens Basalt record the thermal waxing and waning of a major pulse of basalt interacting with the crust. The intensity of the thermal input of this event is indirectly recorded in the volume of basalt erupted. The earliest stage of the Steens Basalt (lower A) is dominated by low-volume magma flux and fractionation, but the latter part of that stage becomes more homogenous and represents the onset of the early waxing stage of voluminous magma generation. This initial stage gives way to one of rapid magma input and frequent eruption (lower B Steens Basalt), leading to an increasingly mafic magma system dominated by basaltic recharge that outpaces differentiation and contributes to substantial warming of the crust. Differentiation begins to outpace recharge toward the end of the lower B Steens Basalt stage, signaling initiation of the waning period. Now well established, the magmatic system becomes more evolved during the upper Steens Basalt stage, with more time between eruptions and more differentiated compositions indicating reduced basaltic recharge. Crustal assimilation becomes more abundant as the crust is thermally primed; pulses of accom-

panying felsic magmatism are consistent with a dominant role for crystallization and crustal assimilation. Within each of these stages of the Steens Basalt, a "perched" magma system is established, whereby the system continually evolves to an equilibrium state after perturbations to the system in the form of recharge, mixing, and/or assimilation. As CRBG magmatism migrates north, a comparable pulse of magmatism occurs, represented by the Imnaha and Grande Ronde Basalts.

Chemostratigraphic changes comparable to the Steens Basalt and CRBG are evident in the Deccan Traps, Siberian Traps, and in the Bushveld and Stillwater LMI. Each likely records an early stage of recharge dominance over fractionation, and a later stage of fractionation coupled with crustal melting and assimilation. Few published studies of CFB provide the detailed stratigraphic control presented here for the Steens Basalt. The generalized comparisons we make to other CFB are a first step toward identifying similarities in petrogenetic evolution among these mafic systems. If oceanic LIP volumes are equivalent to the entire intrusive/extrusive volume of CFB, and LMI roughly represent the intrusive counterparts to CFB remaining in the crust, the proportions suggest that at least 50%–85% of the magma volumes at CFB remain in the crust, effectively remaking the crust of these regions into mafic compositions.

ACKNOWLEDGMENTS

Funding for this project was provided by the National Science Foundation (EAR 1427716, 1427737) and a Geological Society of America graduate student research grant. The authors would like to thank John Wolff and Vic Camp for their thoughtful reviews that greatly improved this manuscript. Our sincere gratitude to Dan Miggins, Anthony Koppers, and Susan Schnur of the Oregon State University Argon Geochronology Lab, Corvallis, Oregon, USA, for invaluable assistance with all the required steps of the Ar-Ar dating process. Thanks also go to Frank Tepley for the many hours of assistance and advice provided in the Oregon State University Electron Microprobe Laboratory.

REFERENCES CITED

Annells, R.N., 1973, Proterozoic flood basalts of eastern Lake Superior: The Keweenawan volcanic rocks of the Mamainse Point area, Ontario: Geological Survey of Canada, Paper 72-10, 51 p., https://doi.org/10.4095/102486.

Baksi, A.K., 2013, Timing and duration of volcanism in the Columbia River Basalt Group: A review of existing radiometric data and new constraints on the age of the Steens through Wanapum Basalt extrusion, *in* Reidel, S.P., Camp, V.E., Ross, M.E., Wolff, J.A., Martin, B.S., Tolan, T.L., and Wells, R.E., eds., The Columbia River Flood Basalt Province: Geological Society of America Special Paper 497, p. 67–85, https://doi.org/10.1130/2013.2497(03).

Barnes, S.J., Maier, W.D., and Curl, E.A., 2010, Composition of the marginal rocks and sills of the Rustenburg Layered Suite, Bushveld Complex, South Africa: Implications for the formation of the platinum-group element deposits: Economic Geology, v. 105, p. 1491–1511, https://doi.org/10.2113/econgeo.105.8.1491.

Barry, T.L., Kelley, S.P., Reidel, S.P., Camp, V.E., Self, S., Jarboe, N.A., Duncan, R.A., and Renne, P.R., 2013, Eruption chronology of the Columbia River Basalt Group, *in* Reidel, S.P., Camp, V.E., Ross, M.E., Wolff, J.A., Martin, B.S., Tolan, T.L., and Wells, R.E., eds., The Columbia River Flood Basalt Province: Geological Society of America Special Paper 497, p. 45–66, https://doi.org/10.1130/2013.2497(02).

Beane, J.E., Turner, C.A., Hooper, P.R., Subbarao, K.V., and Walsh, J.N., 1986, Stratigraphy, composition and form of the Deccan Basalts, Western Ghats, India: Bulletin of Volcanology, v. 48, p. 61–83, https://doi.org/10.1007/BF01073513.

Bendaña, S.J., 2016, Documenting mantle and crustal contributions to flood basalt magmatism via computational modeling of the Steens Basalt, southeast Oregon [M.S. thesis]: Central Washington University, Ellensburg, Washington, USA, 183 p.

Bendaña, S., Bohrson, W.A., Graubard, M.A., Moore, N.E., and Grunder, A.L., 2017, Quantification of Mantle vs. Crustal Contributions to the Steens Flood Basalt Magmatic System: Abstract ME23C-070 presented at 2017 Scientific Assembly of the International Association of Volcanology and Chemistry of the Earth's Interior (IAVCEI), Portland, Oregon, USA, 14–18 August.

Benson, T.R., and Mahood, G.A., 2016, Geology of the Mid-Miocene Rooster Comb Caldera and Lake Owyhee Volcanic Field, eastern Oregon: Silicic volcanism associated with Grande Ronde flood basalt: Journal of Volcanology and Geothermal Research, v. 309, p. 96–117, https://doi.org/10.1016/j.jvolgeores.2015.11.011.

Benson, T.R., Mahood, G.A., and Grove, M., 2017, Geology and $^{40}Ar/^{39}Ar$ geochronology of the middle Miocene McDermitt volcanic field, Oregon and Nevada: Silicic volcanism associated with propagating flood basalt dikes at initiation of the Yellowstone hotspot: Geological Society of America Bulletin, v. 129, p. 1027–1051, https://doi.org/10.1130/B31642.1.

Bondre, N.R., and Hart, W.K., 2008, Morphological and textural diversity of the Steens Basalt lava flows, Southeastern Oregon, USA: Implications for emplacement style and nature of eruptive episodes: Bulletin of Volcanology, v. 70, no. 8, p. 999–1019, https://doi.org/10.1007/s00445-007-0182-x.

Bondre, N.R., Duraiswami, R.A., and Dole, G., 2004, Morphology and emplacement of flows from the Deccan Volcanic Province, India: Bulletin of Volcanology, v. 66, p. 29–45, https://doi.org/10.1007/s00445-003-0294-x.

Brown, R.J., Blake, S., Bondre, N.R., Phadnis, V.M., and Self, S., 2011, ´A´ ā lava flows in the Deccan Volcanic Province, India, and their significance for the nature of continental flood basalt eruptions: Bulletin of Volcanology, v. 73, p. 737–752, https://doi.org/10.1007/s00445-011-0450-7.

Brueseke, M.E., Heizler, M.T., Hart, W.K., and Mertzman, S.A., 2007, Distribution and geochronology of Oregon Plateau (USA) flood basalt volcanism: The Steens Basalt revisited: Journal of Volcanology and Geothermal Research, v. 161, p. 187–214, https://doi.org/10.1016/j.jvolgeores.2006.12.004.

Bryan, S.E., Peate, I.U., Peate, D.W., Self, S., Jerram, D.A., Mawby, M.R., and Miller, J.A., 2010, The largest volcanic eruptions on Earth: Earth-Science Reviews, v. 102, p. 207–229, https://doi.org/10.1016/j.earscirev.2010.07.001.

Burgess, S.D., and Bowring, S.A., 2015, High-precision geochronology confirms voluminous magmatism before, during, and after Earth's most severe extinction: Science Advances, v. 1, e1500470, https://doi.org/10.1126/sciadv.1500470.

Burgess, S.D., Muirhead, J.D., and Bowring, S.A., 2017, Initial pulse of Siberian Traps sills as the trigger of the end-Permian mass extinction: Nature Communications, v. 8, https://doi.org/10.1038/s41467-017-00083-9.

Camp, V.E., and Hanan, B.B., 2008, A plume-triggered delamination origin for the Columbia River Basalt Group: Geosphere, v. 4, no. 3, p. 480–495, https://doi.org/10.1130/GES00175.1.

Camp, V.E., and Ross, M.E., 2004, Mantle dynamics and genesis of mafic magmatism in the intermontane Pacific Northwest: Journal of Geophysical Research. Solid Earth, v. 109, https://doi.org/10.1029/2003JB002838.

Camp, V.E., Ross, M.E., and Hanson, W.E., 2003, Genesis of flood basalts and Basin and Range volcanic rocks from Steens Mountain to the Malheur River Gorge, Oregon: Geological Society of America Bulletin, v. 115, p. 105–128, https://doi.org/10.1130/0016-7606(2003)115<0105:GOFBAB>2.0.CO;2.

Camp, V.E., Ross, M.E., Duncan, R.A., Jarboe, N.A., Coe, R.S., Hanan, B.B., and Johnson, J.A., 2013, The Steens Basalt: Earliest lavas of the Columbia River Basalt Group, *in* Reidel, S.P., Camp, V.E., Ross, M.E., Wolff, J.A., Martin, B.S., Tolan, T.L., and Wells, R.E., eds., The Columbia River Flood Basalt Province: Geological Society of America Special Paper 497, p. 87–116, https://doi.org/10.1130/2013.2497(04).

Carlson, R.W., 1984, Isotopic constraints on Columbia River flood basalt genesis and the nature of the subcontinental mantle: Geochimica et Cosmochimica Acta, v. 48, p. 2357–2372, https://doi.org/10.1016/0016-7037(84)90231-X.

Carlson, R.W., and Hart, W.K., 1987, Crustal genesis on the Oregon Plateau: Journal of Geophysical Research-Solid Earth and Planets, v. 92, no. B7, p. 6191–6206, https://doi.org/10.1029/JB092iB07p06191.

Carlson, R.W., Lugmair, G.W., and Macdougall, J.D., 1981, Columbia River volcanism: The question of mantle heterogeneity or crustal contamination: Geochimica et Cosmochimica Acta, v. 45, p. 2483–2499, https://doi.org/10.1016/0016-7037(81)90100-9.

Cawthorn, R.G., and Davies, G., 1983, Experimental data at 3 kbars pressure on parental magma to the Bushveld Complex: Contributions to Mineralogy and Petrology, v. 83, p. 128–135, https://doi.org/10.1007/BF00373085.

Cawthorn, R.G., and Walraven, F., 1998, Emplacement and crystallization time for the Bushveld Complex: Journal of Petrology, v. 39, p. 1669–1687, https://doi.org/10.1093/petroj/39.9.1669.

Cheng, L.L., Yang, Z.F., Zeng, L., Wang, Y., and Luo, Z.H., 2014, Giant plagioclase growth during storage of basaltic magma in Emeishan Large Igneous Province, SW China: Contributions to Mineralogy and Petrology, v. 167, p. 1–20, https://doi.org/10.1007/s00410-014-0971-0.

Coble, M.A., and Mahood, G.A., 2012, Initial impingement of the Yellowstone plume located by widespread silicic volcanism contemporaneous with Columbia River flood basalts: Geology, v. 40, p. 655–658, https://doi.org/10.1130/G32692.1.

Coffin, M.F., and Eldholm, O., 1994, Large igneous provinces: Crustal structure, dimensions, and external consequences: Reviews of Geophysics, v. 32, p. 1–36, https://doi.org/10.1029/93RG02508.

Coffin, M.F., Duncan, R.A., Eldholm, O., Fitton, J.G., Frey, F.A., Larsen, H.C., Mahoney, J.J., Saunders, A.D., Schlich, R., and Wallace, P.J., 2006, Large igneous provinces and scientific ocean drilling: Status quo and a look ahead: Oceanography, v. 19, p. 150–160, https://doi.org/10.5670/oceanog.2006.13.

Courtillot, V.E., and Renne, P.R., 2003, On the ages of flood basalt events: Comptes Rendus Geoscience, v. 335, p. 113–140, https://doi.org/10.1016/S1631-0713(03)00006-3.

Cox, C., and Keller, G., 2010, Crustal Structure of the High Lava Plains of the Pacific Northwest Source Seismic and Gravity Modeling: Abstract T41E-07 presented at 2010 Fall Meeting, AGU, San Francisco, California, USA, 13–17 December.

Cox, K.G., 1980, A model for flood basalt vulcanism: Journal of Petrology, v. 21, p. 629–650, https://doi.org/10.1093/petrology/21.4.629.

Eagar, K.C., Fouch, M.J., and James, D.E., 2010, Receiver function imaging of upper mantle complexity beneath the Pacific Northwest, United States: Earth and Planetary Science Letters, v. 297, no. 1, p. 141–153, https://doi.org/10.1016/j.epsl.2010.06.015.

Eagar, K.C., Fouch, M.J., James, D.E., and Carlson, R.W., 2011, Crustal structure beneath the High Lava Plains of eastern Oregon and surrounding regions from receiver function analysis: Journal of Geophysical Research. Solid Earth, v. 116, no. B2, https://doi.org/10.1029/2010JB007795.

Eales, H.V., Marsh, J.S., Mitchell, A.A., De Klerk, W.J., Kruger, F.J., and Field, M., 1986, Some geochemical constraints upon models for the crystallization of the Upper Critical Zone Main Zone interval, northwestern Bushveld Complex: Mineralogical Magazine, v. 50, p. 567–582, https://doi.org/10.1180/minmag.1986.050.358.03.

Fedorenko, V.A., Lightfoot, P.C., Naldrett, A.J., Czamanske, G.K., Hawkesworth, C.J., Wooden, J.L., and Ebel, D.S., 1996, Petrogenesis of the flood-basalt sequence at Noril'sk, North Central Siberia: International Geology Review, v. 38, p. 99–135, https://doi.org/10.1080/00206819709465327.

Gao, H., Humphreys, E.D., Yao, H., and van der Hilst, R.D., 2011, Crust and lithosphere structure of the northwestern U.S. with ambient noise tomography: Terrane accretion and Cascade arc development: Earth and Planetary Science Letters, v. 304, p. 202–211, https://doi.org/10.1016/j.epsl.2011.01.033.

Garfunkel, Z., 2008, Formation of continental flood volcanism—The perspective of setting of melting: Lithos, v. 100, no. 1–4, p. 49–65, https://doi.org/10.1016/j.lithos.2007.06.015.

Graubard, M., 2016, Evolution of a Flood Basalt Crustal Magmatic System: In Situ Mineral Data and Computational Modeling of the Steens Basalt [M.S. thesis]: Central Washington University, Ellensburg, Washington, USA, 190 p.

Grove, T.L., Elkins-Tanton, L.T., Parman, S.W., Chatterjee, N., Müntener, O., and Gaetani, G.A., 2003, Fractional crystallization and mantle-melting controls on calc-alkaline differentiation trends: Contributions to Mineralogy and Petrology, v. 145, p. 515–533, https://doi.org/10.1007/s00410-003-0448-z.

Gualda, G.A., Ghiorso, M.S., Lemons, R.V., and Carley, T.L., 2012, Rhyolite-MELTS: A modified calibration of MELTS optimized for silica-rich, fluid-bearing magmatic systems: Journal of Petrology, v. 53, p. 875–890, https://doi.org/10.1093/petrology/egr080.

Gunn, B.M., and Watkins, N.D., 1970, Geochemistry of the Steens Mountain Basalts, Oregon: Geological Society of America Bulletin, v. 81, p. 1497–1516, https://doi.org/10.1130/0016-7606(1970)81[1497:GOTSMB]2.0.CO;2.

Hawkesworth, C., Kelley, S., Turner, S., Le Roex, A., and Storey, B., 1999, Mantle processes during Gondwana break-up and dispersal: Journal of African Earth Sciences, v. 28, no. 1, p. 239–261, https://doi.org/10.1016/S0899-5362(99)00026-3.

Helz, R.T., 1985, Compositions of fine-grained mafic rocks from sills and dikes associated with the Stillwater Complex, *in* Czamanske, G.K., and Zientek, M.L., eds., The Stillwater Complex, Montana: Montana Bureau of Mines and Geology Special Publication 92, p. 97–117.

Helz, R.T., 1995, The Stillwater Complex, Montana: A subvolcanic magma chamber?: The American Mineralogist, v. 80, p. 1343–1346, https://doi.org/10.2138/am-1995-11-1225.

Henry, C.D., Castor, S.B., Starkel, W.A., Ellis, B.S., Wolff, J.A., Laravie, J.A., McIntosh, W.C., and Heizler, M.T., 2017, Geology and evolution of the McDermitt caldera, northern Nevada and southeastern Oregon, western USA: Geosphere, v. 13, p. 1066–1112, https://doi.org/10.1130/GES01454.1.

Higgins, M.D., and Chandrasekharam, D., 2007, Nature of sub-volcanic magma chambers, Deccan Province, India: Evidence from quantitative textural analysis of plagioclase megacrysts in the Giant Plagioclase Basalts: Journal of Petrology, v. 48, p. 885–900, https://doi.org/10.1093/petrology/egm005.

Hofmann, A., 1997, Mantle geochemistry: The message from oceanic volcanism: Nature, v. 385, no. 6613, p. 219–229, https://doi.org/10.1038/385219a0.

Hooper, P.R., 1982, The Columbia River Basalts: Science, v. 215, p. 1463–1468, https://doi.org/10.1126/science.215.4539.1463.

Hooper, P.R., 1984, Physical and chemical constraints on the evolution of the Columbia River basalt: Geology, v. 12, p. 495–499, https://doi.org/10.1130/0091-7613(1984)12<495:PACCOT>2.0.CO;2.

Hooper, P.R., 1988, Crystal fractionation and recharge (RFC) in the American Bar flows of the Imnaha Basalt, Columbia River Basalt Group: Journal of Petrology, v. 29, p. 1097–1118, https://doi.org/10.1093/petrology/29.5.1097.

Hooper, P.R., 2000, Chemical discrimination of Columbia River basalt flows: Geochemistry Geophysics Geosystems, v. 1, no. 6, https://doi.org/10.1029/2000GC000040.

Hooper, P.R., Kleck, W.D., Knowles, C.R., Reidel, S.P., and Thiessen, R.L., 1984, Imnaha Basalt, Columbia River Basalt Group: Journal of Petrology, v. 25, p. 473–500, https://doi.org/10.1093/petrology/25.2.473.

Hooper, P.R., Binger, G.B., and Lees, K.R., 2002, Ages of the Steens and Columbia River flood basalts and their relationship to extension-related calc-alkalic volcanism in eastern Oregon: Geological Society of America Bulletin, v. 114, no. 1, p. 43–50, https://doi.org/10.1130/0016-7606(2002)114<0043:AOTSAC>2.0.CO;2.

Hooper, P.R., Camp, V.E., Reidel, S.P., and Ross, M.E., 2007, The origin of the Columbia River flood basalt province: Plume versus nonplume models, *in* Foulger, G.R., and Jurdy, D.M., eds., Plates, Plumes and Planetary Processes: Geological Society of America Special Paper 430, p. 635–668, https://doi.org/10.1130/2007.2430(30).

Jarboe, N.A., Coe, R.S., Renne, P.R., Glen, J.M.G., and Mankinen, E.A., 2008, Quickly erupted volcanic sections of the Steens Basalt, Columbia River Basalt Group: Secular variation, tectonic rotation, and the Steens Mountain reversal: Geochemistry Geophysics Geosystems, v. 9, no. 11, https://doi.org/10.1029/2008GC002067.

Jarboe, N.A., Coe, R.S., Renne, P.R., and Glen, J.M.G., 2010, The age of the Steens reversal and the Columbia River Basalt Group: Chemical Geology, v. 274, no. 3–4, p. 158–168, https://doi.org/10.1016/j.chemgeo.2010.04.001.

Johnson, D.M., Hooper, P.R., and Conrey, R.M., 1999, XRF analysis of rocks and minerals for major and trace elements on a single low dilution Li-tetraborate fused bead: Advances in X-ray Analysis, v. 41, p. 843–867.

Johnson, J.A., Hawkesworth, C.J., Hooper, P.R., and Binger, G.B., 1998, Major and Trace Element Analyses of Steens Basalt, Southeastern Oregon: U.S. Geological Survey Open-File Report 98-482, 26 p.

Jordan, B.T., Grunder, A.L., Duncan, R.A., and Deino, A.L., 2004, Geochronology of age-progressive volcanism of the Oregon High Lava Plains: Implications for the plume interpretation of Yellowstone: Journal of Geophysical Research: Solid Earth, v. 109, B10, https://doi.org/10.1029/2003JB002776.

Kelly, D., 2016, Estimation of analytical error for major, minor and trace elements analyzed by X-ray fluorescence at the Peter Hooper Geoanalytical Laboratory, Washington State University: Geological Society of America Abstracts with Programs, v. 48, no. 7, https://doi.org/10.1130/abs/2016AM-284288.

Kistler, R.W., and Peterman, Z.E., 1973, Variations in Sr, Rb, K, Na, and initial Sr^{87}/Sr^{86} in Mesozoic granitic rocks and intruded wall rocks in central California: Geological Society of America Bulletin, v. 84, p. 3489–3512, https://doi.org/10.1130/0016-7606(1973)84<3489:VISRKN>2.0.CO;2.

Klewin, K.W., and Berg, J.H., 1991, Petrology of the Keweenawan Mamainse Point lavas, Ontario: Petrogenesis and continental rift evolution: Journal of Geophysical Research. Solid Earth, v. 96, p. 457–474, https://doi.org/10.1029/90JB02089.

Knaack, C., Cornelius, S.B., and Hooper, P.R., 1994, Trace element analyses of rocks and minerals by ICP-MS: Peter Hooper GeoAnalytical Lab, Washington State University, Pullman, Washington, USA, Open-File Report.

Koppers, A.A., Gowen, M.D., Colwell, L.E., Gee, J.S., Lonsdale, P.F., Mahoney, J.J., and Duncan, R.A., 2011, New $^{40}Ar/^{39}Ar$ age progression for the Louisville hot spot trail and implications for inter-hot spot motion: Geochemistry Geophysics Geosystems, v. 12, https://doi.org/10.1029/2011GC003804.

Kuiper, K.F., Deino, A., Hilgen, F.J., Krijgsman, W., Renne, P.R., and Wijbrans, J.R., 2008, Synchronizing rock clocks of Earth history: Science, v. 320, p. 500–504, https://doi.org/10.1126/science.1154339.

Lepage, L., 2003, ILMAT: An Excel worksheet for ilmenite-magnetite geothermometry and geobarometry: Computers & Geosciences, v. 29, p. 673–678, https://doi.org/10.1016/S0098-3004(03)00042-6.

Lightfoot, P.C., Hawkesworth, C.J., and Sethna, S.F., 1987, Petrogenesis of rhyolites and trachytes from the Deccan Trap: Sr, Nd and Pb isotope and trace element evidence: Contributions to Mineralogy and Petrology, v. 95, p. 44–54, https://doi.org/10.1007/BF00518029.

Long, P.E., and Wood, B.J., 1986, Structures, textures, and cooling histories of Columbia River basalt flows: Geological Society of America Bulletin, v. 97, p. 1144–1155, https://doi.org/10.1130/0016-7606(1986)97<1144:STACHO>2.0.CO;2.

Luttinen, A.V., Leat, P.T., and Furnes, H., 2010, Björnnutane and Sembberget basalt lavas and the geochemical provinciality of Karoo magmatism in western Dronning Maud Land, Antarctica: Journal of Volcanology and Geothermal Research, v. 198, no. 1–2, p. 1–18, https://doi.org/10.1016/j.jvolgeores.2010.07.011.

Mahood, G.A., and Benson, T.R., 2017, Using $^{40}Ar/^{39}Ar$ ages of intercalated silicic tuffs to date flood basalts: Precise ages for Steens Basalt Member of the Columbia River Basalt Group: Earth and Planetary Science Letters, v. 459, p. 340–351, https://doi.org/10.1016/j.epsl.2016.11.038.

Mankinen, E.A., Larson, E.E., Gromme, C.S., Prevot, M., and Coe, R.S., 1987, The Steens Mountain (Oregon) Geomagnetic Polarity Transition: 3. Its regional significance: Journal of Geophysical Research, v. 92, no. B8, p. 8057–8076, https://doi.org/10.1029/JB092iB08p08057.

McBirney, A.R., and Noyes, R.M., 1979, Crystallization and layering of the Skaergaard intrusion: Journal of Petrology, v. 20, p. 487–554, https://doi.org/10.1093/petrology/20.3.487.

McCallum, I.S., Raedeke, L.D., and Mathez, E.A., 1980, Investigations of the Stillwater Complex: Part I. Stratigraphy and structure of the banded zone: American Journal of Science, v. 280, p. 59–87.

Minor, S.A., Rytuba, J.J., Goeldner, C.A., and Tegtmeyer, K.J., 1987a, Geologic map of the Alvord Hot Springs quadrangle, Harney County, Oregon: U.S. Geological Survey Miscellaneous Field Studies Map MF-1916, scale 1:24,000.

Minor, S.A., Rytuba, J.J., Meulen, D.B., Grubensky, M.J., and Tegtmeyer, K.J., 1987b, Geologic map of the Wildhorse Lake quadrangle, Harney County, Oregon: U.S. Geological Survey Miscellaneous Field studies Map MF-1915, scale 1:24,000.

Moore, N.E., Lytle, K., Bohrson, W.A., and Grunder, A.L., 2015, New Petrologic and Geochemical Insights into Differentiation Processes Required to Produce the Lower Steens Basalt, Columbia River Basalt Province, SE Oregon: Abstract V41C-3090 presented at 2015 Fall Meeting, AGU, San Francisco, California, USA, 14–18 December.

Neave, D.A., and Putirka, K.D., 2017, A new clinopyroxene-liquid barometer, and implications for magma storage pressures under Icelandic rift zones: The American Mineralogist, v. 102, p. 777–794, https://doi.org/10.2138/am-2017-5968.

Peate, D.W., 1997, The Paraná-Etendeka Province, *in* Mahoney, J.J., and Coffin, M.F., eds., Large Igneous Provinces: Continental, Oceanic, and Planetary Flood Volcanism: American Geophysical Union Geophysical Monograph Series, v. 100, p. 217–245.

Pierce, K.L., and Morgan, L.A., 2009, Is the track of the Yellowstone hotspot driven by a deep mantle plume–Review of volcanism, faulting, and uplift in light of new data: Journal of Volcanology and Geothermal Research, v. 188, p. 1–25, https://doi.org/10.1016/j.jvolgeores.2009.07.009.

Putirka, K.D., 2008, Thermometers and barometers for volcanic systems: Reviews in Mineralogy and Geochemistry, v. 69, p. 61–120, https://doi.org/10.2138/rmg.2008.69.3.

Raedeke, L.D., and McCallum, I.S., 1984, Investigations in the Stillwater complex: Part II. Petrology and petrogenesis of the ultramafic series: Journal of Petrology, v. 25, p. 395–420, https://doi.org/10.1093/petrology/25.2.395.

Rampino, M.R, and Self, S., 2015, Large igneous provinces and biotic extinctions, *in* Sigurdsson, H., Houghton, B., McNutt, S., Rymer, H., and Stix, J., eds., The Encyclopedia of Volcanoes: Elsevier, p. 1049–1058.

Ramos, F.C., Wolff, J.A., Starkel, W., Eckberg, A., Tollstrup, D.L., and Scott, S., 2013, The changing nature of sources associated with Columbia River flood basalts: Evidence from strontium isotope ratio variations in plagioclase phenocrysts, *in* Reidel, S.P., and Hooper, P.R., eds., Volcanism and Tectonism in the Columbia River Flood-Basalt Province: Geological Society of America Special Paper 239, p. 231–257, https://doi.org/10.1130/2013.2497(09).

Reichow, M.K., Pringle, M.S., Al'Mukhamedov, A.I., Allen, M.B., Andreichev, V.L., Buslov, M.M., Davies, C.E., Fedosee, G.S., Fitton, J.G., Inger, S., Medvedev, A.Ya., Mitchell, C., Puchkov, V.N., Safonova, I.Yu., Scott, R.A., and Saunders, A.D., 2009, The timing and extent of the eruption of the Siberian Traps large igneous province: Implications for the end-Permian environmental crisis: Earth and Planetary Science Letters, v. 277, p. 9–20, https://doi.org/10.1016/j.epsl.2008.09.030.

Reidel, S.P., and Tolan, T.L., 2013, The Grande Ronde Basalt, Columbia River Basalt Group, *in* Reidel, S.P., Camp, V.E., Ross, M.E., Wolff, J.A., Martin, B.S., Tolan, T.L., and Wells, R.E., eds., The Columbia River Flood Basalt Province: Geological Society of America Special Paper 497, p. 117–153, https://doi.org/10.1130/2013.2497(05).

Reidel, S.P., Fecht, K.R., Hagood, M.C., Tolan, T.L., and Hooper, P.R., 1989a, The geologic evolution of the central Columbia Plateau, *in* Reidel, S.P., and Hooper, P.R., eds., Volcanism and Tectonism in the Columbia River Flood-Basalt Province: Geological Society of America Special Paper 239, p. 247–264, https://doi.org/10.1130/SPE239-p247.

Reidel, S.P., Tolan, T.L., Hooper, P.R., Beeson, M.H., Fecht, K.R., Bentley, R.D., and Anderson, J.L., 1989b, The Grande Ronde Basalt, Columbia River Basalt Group; Stratigraphic descriptions and correlations in Washington, Oregon, and Idaho, *in* Reidel, S.P., and Hooper, P.R., eds., Volcanism and Tectonism in the Columbia River Flood-Basalt Province: Geological Society of America Special Paper 239, p. 21–54, https://doi.org/10.1130/SPE239-p21.

Reidel, S.P., Camp, V.E., Tolan, T.L., and Martin, B.S., 2013, The Columbia River flood basalt province: Stratigraphy, areal extent, volume, and physical volcanology, *in* Reidel, S.P., Camp, V.E., Ross, M.E., Wolff, J.A., Martin, B.S., Tolan, T.L., and Wells, R.E., eds., The Columbia River Flood Basalt Province: Geological Society of America Special Paper 497, p. 1–43, https://doi.org/10.1130/2013.2497(01).

Reiners, P.W., Nelson, B.K., and Ghiorso, M.S., 1995, Assimilation of felsic crust by basaltic magma: Thermal limits and extents of crustal contamination of mantle-derived magmas: Geology, v. 23, p. 563–566, https://doi.org/10.1130/0091-7613(1995)023<0563:AOFCBB>2.3.CO;2.

Renne, P.R., Sprain, C.J., Richards, M.A., Self, S., Vanderkluysen, L., and Pande, K., 2015, State shift in Deccan volcanism at the Cretaceous-Paleogene boundary, possibly induced by impact: Science, v. 350, p. 76–78, https://doi.org/10.1126/science.aac7549.

Richards, M.A., Alvarez, W., Self, S., Karlstrom, L., Renne, P.R., Manga, M., Sprain, C.J., Smit, J., Vanderkluden, L., and Gibson, S.A., 2015, Triggering of the largest Deccan eruptions by the Chicxulub impact: Geological Society of America Bulletin, v. 127, p. 1507–1520, https://doi.org/10.1130/B31167.1.

Rytuba, J.J., 1988, Volcanism, extensional tectonics, and epithermal mineralization in the Northern Basin and Range Province, California, Nevada, Oregon, and Idaho: Geological Survey Circular, v. 1035, p. 59–62.

Sawlan, M.G., 2017, Alteration, mass analysis, and magmatic compositions of the Sentinel Bluffs Member, Columbia River flood basalt province: Geosphere, v. 14, p. 286–303, https://doi.org/10.1130/GES01188.1.

Self, S., Thordarson, T., Keszthelyi, L., Walker, G.P.L., Hon, K., Murphy, M.T., and Finnemore, S., 1996, A new model for the emplacement of Columbia River basalts as large, inflated pahoehoe lava flow fields: Geophysical Research Letters, v. 23, p. 2689–2692, https://doi.org/10.1029/96GL02450.

Self, S., Widdowson, M., Thordarson, T., and Jay, A.E., 2006, Volatile fluxes during flood basalt eruptions and potential effects on the global environment: A Deccan perspective: Earth and Planetary Science Letters, v. 248, no. 1, p. 518–532, https://doi.org/10.1016/j.epsl.2006.05.041.

Self, S., Schmidt, A., and Mather, T.A., 2014, Emplacement characteristics, time scales, and volcanic gas release rates of continental flood basalt eruptions on Earth, *in* Keller, G., and Kerr, A.C., eds., Volcanism, Impacts, and Mass Extinctions: Causes and Effects: Geological Society of America Special Paper 505, p. 319–337, https://doi.org/10.1130/2014.2505(16).

Sharma, M., 1997, Siberian Traps, *in* Mahoney, J.J, and Coffin, M.J., eds., Large Igneous Provinces: American Geophysical Union Geophysical Monograph, v. 100, p. 273–295.

Shervais, J.W., Vetter, S.K., and Hanan, B.B., 2006, Mafic layered sill complex beneath the eastern Snake River Plain: Evidence from cyclic geochemical variations in basalt: Geology, v. 34, no. 5, p. 365–368, https://doi.org/10.1130/G22226.1.

Sheth, H., 2016, Giant plagioclase basalts: Continental flood basalt-induced remobilization of anorthositic mushes in a deep crustal sill complex: Geological Society of America Bulletin, v. 128, p. 916–925, https://doi.org/10.1130/B31404.1.

Streck, M.J., and Grunder, A.L., 2012, Temporal and crustal effects on differentiation of tholeiite to calcalkaline and ferro-trachytic suites, High Lava Plains, Oregon, USA: Geochemistry Geophysics Geosystems, v. 13, no. 11, https://doi.org/10.1029/2012GC004237.

Streck, M.J., Ferns, M.L., and McIntosh, W., 2015, Large, persistent rhyolitic magma reservoirs above Columbia River Basalt storage sites: The Dinner Creek Tuff Eruptive Center, eastern Oregon: Geosphere, v. 2, p. 1–10, https://doi.org/10.1130/GES01086.1.

Streck, M.J., McIntosh, W., and Ferns, M.L., 2016, Co-CRBG rhyolite volcanism reassessed: Geological Society of America Abstracts with Programs, v. 48, no. 6, https://doi.org/10.1130/abs/2016RM-276108.

Subbarao, K.V., and Hooper, P.R., 1988, Reconnaissance map of the Deccan Basalt Group in the Western Ghats, India, *in* Subbarao, K.V., ed., Deccan Flood Basalts: Geological Society of India Memoir 10 (enclosure).

Takahahshi, E., Nakajima, K., and Wright, T.L., 1998, Origin of the Columbia River basalts: Melting model of a heterogeneous plume head: Earth and Planetary Science Letters, v. 162, no. 1, p. 63–80, https://doi.org/10.1016/S0012-821X(98)00157-5.

Talusani, R.V.R., 2012, Giant plagioclase basalts from northeastern Deccan volcanic province, India: Implications for their origin and petrogenetic significance: International Journal of Geosciences, v. 3, p. 1027–1032, https://doi.org/10.4236/ijg.2012.35103.

Thompson, R., Morrison, M., Dickin, A., and Hendry, G., 1983, Continental flood basalts...arachnids rule OK?, *in* Hawkesworth, C.L., and Norry, M.J., eds., Continental Basalts and Mantle Xenoliths: Nantwich, UK, Shiva Publishing Ltd., p. 158–185.

Turner, S., Hawkesworth, C., Gallagher, K., Stewart, K., Peate, D., and Mantovani, M., 1996, Mantle plumes, flood basalts, and thermal models for melt generation beneath continents: Assessment of a conductive heating model and application to the Paraná: Journal of Geophysical Research. Solid Earth, v. 101, no. B5, p. 11503–11518, https://doi.org/10.1029/96JB00430.

Twist, D., and French, B.M., 1983, Voluminous acid volcanism in the Bushveld Complex: A review of the Rooiberg Felsite: Bulletin of Volcanology, v. 46, p. 225–242, https://doi.org/10.1007/BF02597559.

Wager, L.R., and Brown, G.M., 1967, Layered Igneous Rocks: San Francisco, California, USA, W.H. Freeman and Company, 588 p.

Wagner, L., Forsyth, D.W., Fouch, M.J., and James, D.E., 2010, Detailed three-dimensional shear wave velocity structure of the northwestern United States from Rayleigh wave tomography: Earth and Planetary Science Letters, v. 299, no. 3, p. 273–284, https://doi.org/10.1016/j.epsl.2010.09.005.

Walker, G.P.L., 1971, Compound and simple lava flows and flood basalts: Bulletin Volcanologique, v. 35, p. 579–590, https://doi.org/10.1007/BF02596829.

Walker, G.W., and MacLeod, N.S., 1991, Geologic Map of Oregon: U.S. Geological Survey, scale 1:500,000, 2 sheets.

Warren, L.M., Snoke, J.A., and James, D.E., 2008, S-wave velocity structure beneath the High Lava Plains, Oregon, from Rayleigh-wave dispersion inversion: Earth and Planetary Science Letters, v. 274, no. 1–2, p. 121–131, https://doi.org/10.1016/j.epsl.2008.07.014.

Wells, R., Bukry, D., Friedman, R., Pyle, D., Duncan, R., Haeussler, P., and Wooden, J., 2014, Geologic history of Siletzia, a large igneous province in the Oregon and Washington Coast Range: Correlation to the geomagnetic polarity time scale and implications for a long-lived Yellowstone hotspot: Geosphere, v. 10, p. 692–719, https://doi.org/10.1130/GES01018.1.

Whiteside, J.H., Olsen, P.E., Eglinton, T., Brookfield, M.E., and Sambrotto, R.N., 2010, Compound-specific carbon isotopes from Earth's largest flood basalt eruptions directly linked to the end-Triassic mass extinction: Proceedings of the National Academy of Sciences of the United States of America, v. 107, no. 15, p. 6721–6725, https://doi.org/10.1073/pnas.1001706107.

Wolff, J.A., and Ramos, F.C., 2013, Source materials for the main phase of the Columbia River Basalt Group: Geochemical evidence and implications for magma storage and transport, *in* Reidel, S.P., Camp, V.E., Ross, M.E., Wolff, J.A., Martin, B.S., Tolan, T.L., and Wells, R.E., eds., The Columbia River Flood Basalt Province: Geological Society of America Special Paper 497, p. 273–291, https://doi.org/10.1130/2013.2497(11).

Wolff, J.A., Ramos, F.C., Hart, G.L., Patterson, J.D., and Brandon, A.D., 2008, Columbia River flood basalts from a centralized crustal magmatic system: Nature Geoscience, v. 1, no. 3, p. 177–180, https://doi.org/10.1038/ngeo124.

Yudovskaya, M.A., Kinnaird, J.A., Sobolev, A.V., Kuzmin, D.V., McDonald, I., and Wilson, A.H., 2013, Petrogenesis of the Lower Zone olivine-rich cumulates beneath the Platreef and their correlation with recognized occurrences in the Bushveld Complex: Economic Geology, v. 108, p. 1923–1952.